HHS Public Access

Author manuscript

Nat Cardiovasc Res. Author manuscript; available in PMC 2023 June 09.

Published in final edited form as:

Nat Cardiovasc Res. 2022 August ; 1(8): 775–790. doi:10.1038/s44161-022-00114-9.

Blood flow modeling reveals improved collateral artery performance during the regenerative period in mammalian hearts

Suhaas Anbazhakan[1,8], **Pamela E. Rios Coronado**[2,8], **Ana Natalia L. Sy-Quia**[2], **Lek Wei Seow**[2], **Aubrey M. Hands**[2], **Mingming Zhao**[3,4], **Melody L. Dong**[1], **Martin R. Pfaller**[1,3], **Zhainib A. Amir**[2], **Brian C. Raftrey**[2], **Christopher K. Cook**[2], **Gaetano D'Amato**[2], **Xiaochen Fan**[2], **Ian M. Williams**[2], **Sawan K. Jha**[2], **Daniel Bernstein**[3,4], **Koen Nieman**[5], **Anca M. Pașca**[3], **Alison L. Marsden**[1,3,4,*], **Kristy Red Horse**[2,4,6,7,*]

[1]Department of Bioengineering, Stanford University, Stanford, CA 94305, USA

[2]Department of Biology, Stanford University, Stanford, CA 94305, USA

[3]Department of Pediatrics, Stanford University School of Medicine, Stanford, CA, 94305

[4]Stanford Cardiovascular Institute, Stanford University School of Medicine, Stanford, CA 94305, USA

[5]Departments of Cardiovascular Medicine and Radiology, School of Medicine, Stanford University, Stanford, CA, 94305, USA

[6]Institute for Stem Cell Biology and Regenerative Medicine, Stanford University School of Medicine, Stanford, CA 94305, USA

[7]Howard Hughes Medical Institute, Stanford, CA, 94305, USA

[8]These authors contributed equally

Abstract

Collateral arteries bridge opposing artery branches, forming a natural bypass that can deliver blood flow downstream of an occlusion. Inducing coronary collateral arteries could treat cardiac ischemia, but more knowledge on their developmental mechanisms and functional capabilities is required. Here we used whole-organ imaging and three-dimensional computational fluid dynamics modeling to define spatial architecture and predict blood flow through collaterals in neonate

*Corresponding author: kredhors@stanford.edu (KR-H) and amarsden@stanford.edu (ALM).

Author Contributions Statement

S.A., P.E.R.C., A.L.M., and K.R.H. conceived and designed the project. S.A., P.E.R.C., A.N.L.S.-Q., C.K.C., G.D., X.F., I.M.W., and S.K.J. performed experiments. S.A, P.E.R.C., A.N.L.S.-Q., L.W.S., A.M.H., and Z.A.A. analyzed data. S.A. performed fluid simulations. P.E.R.C., B.C.R., M.Z., and D.B. performed murine cardiac injury studies. K.N. and A.M.P. contributed human adult and fetal samples, respectively. S.A., M.L.D., and M.R.P. provided analysis tools. S.A. and P.E.R.C. prepared figures. S.A., P.E.R.C., A.L.M., and K.R.H. wrote the manuscript.

Code Availability

The code used for flow simulations can be found on the SimVascular github (https://simvascular.github.io/). Custom code for Strahler ordering and volume perfusion using publicly available modules, such as the vascular toolkit, can be found on github (https://github.com/StanfordCBCL/Collateral).

Competing Interests Statement

The authors declare no competing interests.

and adult mouse hearts. Neonate collaterals were more numerous, larger in diameter and more effective at restoring blood flow. Decreased blood flow restoration in adults arose because during postnatal growth coronary arteries expanded by adding branches rather than increasing diameters, altering pressure distributions. In humans, adult hearts with total coronary occlusions averaged 2 large collaterals, with predicted moderate function, while normal fetal hearts showed over 40 collaterals, likely too small to be functionally relevant. Thus, we quantify the functional impact of collateral arteries during heart regeneration and repair–a critical step toward realizing their therapeutic potential.

Introduction

Cardiovascular disease, including coronary artery disease (CAD), is the leading cause of death worldwide[1]. CAD can result in decreased blood flow to the myocardium, jeopardizing cardiac muscle function. Current treatments involve invasive surgical procedures, but a significant number are unsuccessful, especially in diffuse multi-vessel CAD[2]. Humans and other mammals can develop specialized blood vessels called collateral arteries that function as natural coronary bypasses. These are defined as artery segments directly bridging two artery branches without intervening capillaries, directly providing blood flow distal to a coronary blockage. Although only a minority of adult humans have functionally significant collateral arteries, clinical observations indicate that they can successfully shunt blood around a stenosis to protect against myocardial ischemia and reduce the risk of cardiac death[3,4]. Thus, inducing collateral development could be a promising therapeutic approach for treating CAD[5]. However, a roadblock to this goal is the lack of knowledge about collateral development and their ability to restore blood flow.

While studies have characterized the presence or absence of native collateral arteries across different mammals[6], mice are the most common model for investigating their function during cardiac injury, usually through surgically-induced myocardial infarctions (MI)[7–9]. Mice do not have pre-existing collateral arteries, but by 7 days post-MI, 6–10 collaterals (average 18 μm diameter) are observed in adults through Microfil vascular filling[8]. Thus, mice are a useful model for exploring collateral biology.

We recently used a different technique to identify collaterals—whole-mount immunofluorescence—coupled with lineage tracing and mouse genetics to identify mechanisms driving collateral development[7]. In regenerating neonate hearts, collaterals form post-MI when arterial endothelial cells migrate into the infarct zone in response to hypoxia-induced CXCL12 and coalesce into collateral arteries[7]. This process was termed artery reassembly and did not occur in non-regenerative adult hearts, suggesting that the collaterals observed during vascular filling (described above) utilized a different mechanism. Exogenous CXCL12 application induced artery reassembly in adults to create collaterals up to 40 μm in diameter[7]. Although these collaterals were positively correlated with heart regeneration/repair, characterizing blood flow capacity is required to understand their functional capabilities and therapeutic potential.

How structure affects collateral hemodynamics remains unknown due to technical barriers of imaging blood flow. Clinical measurements rely on qualitative assessments from angiograms

or indirect pressure measurements[11]. More accurate measurements in humans are currently invasive and somewhat unreliable since conclusive relationships cannot be made without quantifying all collaterals, many of which are undetectable in angiograms. Visualizing blood flow is extremely difficult in small experimental animals, and collaterals are quantified from *ex-vivo* methods with limitations: 1. Vascular filling (Microfil casting, μCT and fluorescent conjugates)[12], which creates a non-cell specific volumetric map, and 2. Whole-mount immunostaining, which disrupts 3D structure[7]. Neither approach provides a precise picture of blood flow distribution.

Computational fluid dynamics (CFD) modeling can directly and precisely estimate blood flow. CFD allows patient-specific surgical and treatment planning in numerous human cardiovascular diseases[13–17]. CFD estimates difficult to measure hemodynamic forces in animal models[18–20], including the retinal vasculature, thoracic aorta, and feto-placental vessels[21–23], and have been validated via MRI[24,25]. Another advantage of CFD modeling is the ability to systematically alter certain parameters while keeping others constant, leading to rapid conclusions on the reparative capabilities of different vascular architectures[26].

High-resolution images with intact volumetric dimensions are critical to CFD modeling. To date, vascular labeling methods are not suitable for CFD modeling. However, recent innovations in tissue clearing and whole-organ microscopy could provide sufficiently high resolution images[12,27–29]. Thus, CFD is perfectly poised to push forward our understanding of collateral function.

We optimized whole-organ immunostaining/clearing to image the entire intact artery tree and build high-fidelity 3D models of neonate and adult hearts. Flow restoration was measured with virtual occlusions and various collateral configurations. The results showed that naturally forming collaterals in adult mouse hearts restore sub-optimal flow. In contrast, naturally forming collaterals in neonates are highly restorative because structural parameters and cardiac output at this stage results in lower overall pressure loss along the coronary tree. We investigated human collaterals in whole-organ images of fetal hearts and angiograms from patients with chronic coronary occlusions (CTO). Fetal hearts contained greater than 40, while patient angiograms identified an average of 2. Comparisons to CFD mouse models suggested that fetal collaterals may be functionally insignificant and those in patients lie between neonate and adult mouse capabilities. In total, the combination of whole-organ artery labeling with 3D CFD modeling provides a powerful tool to accurately analyze hemodynamic forces in collateral arteries to broaden our understanding of their functional significance and therapeutic potential.

Results

3D imaging of entire neonatal and adult coronary artery tree

To image the entire intact artery tree in three dimensions, a whole-organ immunostaining and clearing method based on iDISCO was optimized for cardiac tissue using postnatal day 6 (P6) mice[12,28], which allowed us to image smooth muscle actin (α-SMA)-positive arterial smooth muscle cells throughout the heart using Light sheet microscopy (Fig. 1a and b). 3D rendering arterial immunolabeling using Imaris software revealed improvements

over previous method[7]. The 3D architecture was retained (Fig. 1c), and the septal artery (SpA) was fully visible in addition to the left (LCA) and right (RCA) coronary arteries (Fig $1c_{ii}$). We could also immunolabel and image intact all arterial vessels (Fig. 1d and e), even deep within the adult septum (Fig. 1f). Co-staining with arterial endothelial marker Connexin40 confirmed extensive overlap (Fig. $1b_{iii\text{-}v}$). Qualitatively, the density of arteries is much greater in adults compared to neonates (Compare Fig. 1a and 1d), and more branches were detected when compared to μCT[30].

To characterize collateral arteries, we imaged hearts from mice subjected to myocardial infarction (MI)(uninjured mouse hearts do not contain collaterals)[7,8]. Injured neonatal hearts were harvested 4-days post-MI, followed by arterial immunolabeling and clearing. A collateral tracing pipeline was developed using neonatal images (Fig. 2a). ImageJ's Simple Neurite Tracer plugin[31,32] was used to trace, in a semi-automated way, every α-SMA+ vessel originating downstream of the LCA occlusion and connecting to either an RCA, SpA, or non-occluded LCA branch (Supplementary Video 1). Traced paths were isolated and masked so that 3D rendering in Imaris created a map of every collateral artery (Fig. 2b, Supplementary Video 1). The resolution of our method allowed us to annotate the precise collateral segments that bridged two artery branches (Fig. $2b_{ii}$). A collateral bridge was defined as the segment of continuous smooth muscle covered vessel that existed between two branch tips with opposing branch angles (Fig. 2c). Importantly, tracing did not detect collateral connections in non-injured neonate hearts (Extended Data Fig. 1).

Collateral arteries form faster in neonates than in adults[7]. When we injured adult mice, and assessed for collaterals 4-days post MI, we observed profound arterial pruning indicating robust injury, but found virtually no α-SMA+ collateral vessels in most hearts (Extended Data Fig. 2a and b). Thus, we compared collateral metrics in injured hearts 4-days post MI for neonates and 28-days post-MI in adults, a time point previously shown to possess the typical number of collaterals in adult hearts[8].

To validate the functionality of α-SMA+ collaterals, we injected rat-anti-mouse CD31 intravenously 30 min prior to euthanasia to label perfused endothelial cells. Hearts were fixed and immunolabeled with α-SMA and donkey-anti-rat antibodies before clearing. All α-SMA+ collaterals arteries were patent since they were also CD31+ (Extended Data Fig. 2d–f, Supplementary Video 2).

To localize collateral bridges with respect to injured myocardium, we labeled all coronary vessels in the neonate with vascular endothelial cell marker, Podocalyxin, and used the autofluorescence to define surviving muscle. Areas lacking autofluorescence, which were not present in uninjured hearts, delineated injured myocardium, which was confirmed by accompanying disrupted vasculature (Fig. 2d, Supplementary Video 3). Injured regions were outlined and overlaid onto collateral models (Fig. $2b_{i}$). Collateral bridges were usually located at the edge of the infarcted area, connecting regions of muscle and vascular death to unaffected sites in the heart (Fig. 2d). At this location, almost half of the collateral bridges were found spanning healthy and infarcted tissue, but many bridges were completely within either healthy or infarcted tissue (Extended Data Fig. 3a and b). Similar patterns were observed in adult hearts (Fig. 2e–g).

We next quantified collateral connection type, numbers, and relative sizes. Collateral connections were categorized based on which artery they connected (Fig. 2h), most often to the SpA. Neonate hearts formed more LCA-LCA and fewer RCA-LCA connections than adults (Fig. 2h). We hypothesized that anatomical proximity could make the SpA more likely to connect with an injured LCA. Measuring the distances between the mid-collateral bridge and the aorta revealed that the SpA forms connections at points closer to its origin than the RCA (Extended Data Fig. 3c). The distal most tips of the SpA in uninjured hearts are also closer (Extended Data Fig. 3d). Measuring the distance between SpA or RCA tips and those of the LCA showed only a mild trend of SpAs being closer (Extended Data Fig. 3e and f). Therefore, the sites where collateral bridges form might be dictated in part by hemodynamic factors resulting from the distance of SpA to the aorta. Neonate hearts also formed approximately 40% more collaterals than adults (Fig. 2i), and their diameters were larger, both absolutely and relative to the proximal LCA (Fig. 2j and data not shown). (Normalization to proximal LCA was performed to account for small differences in individual mouse body size). These data highlight the importance of advanced imaging methods for observing accurate vascular remodeling patterns, i.e., those involving the septal artery, and underscore the significant differences between young and old hearts.

Modeling coronary blood flow

To understand how these collaterals might restore blood flow in the presence of a vascular occlusion, an *in silico* approach was employed to computationally estimate blood flow while manipulating different parameters in isolation, such as collateral number, size, and location. First, an anatomically representative model of the native adult coronary tree was created using the open-source software, SimVascular (www.simvascular.org)[33], from a Light sheet image of a non-injured adult heart labeled with α-SMA (Fig. 3a). The Light sheet images (Fig. $3a_i$) were used as a guide for drawing path lines through every artery in the heart up to tertiary branches (Fig. $3a_{ii}$, Methods). Special care was taken to ensure the only vessels not modeled were downstream of the outlets to the 3D model. Arteries were then segmented by drawing a circle spanning the entire cross-section at even intervals along the vessel (Fig. $3a_{iii}$). The segmentations were lofted into a 3D model (Fig. $3a_{iv}$). We next measured tissue shrinkage during iDISCO by calculating heart volumes pre- and post-clearing (Fig. $3b_i$). Since shrinkage averaged 37% (Fig. $3b_{ii}$), the model was computationally uniformly scaled up by 1.58-fold (Fig. $3b_{iii}$, equation 1 in Methods). The result was a model reflecting the realistic anatomic 3D architecture of an adult mouse coronary artery tree.

This model was then used to computationally estimate physiologically realistic blood flow parameters throughout the arterial network. Simulations first required setting boundary conditions. At the aortic inlet, a flow waveform was set based on experimentally measured blood velocities from the literature for the neonate[34] and adult[35]. Two outlet boundary conditions were set: 1. An RCR Windkessel model representing the systemic circulation at the aortic outlet[36], and 2. A lumped parameter network (LPN) representing the coronary vessels downstream of the 3D model[37,38] (Fig. 3c). The lumped parameters included values accounting for vessel resistance at downstream arteries, capillaries, and veins and intramyocardial pressure due to ventricle contraction (Fig. 3c). Simulations were run on initial estimated parameters (see Methods) and were subsequently tuned to match expected

flow splits between coronary branches to ensure our CFD simulation distributed flow proportionally. Flow splits were calculated based on perfusion territories for each of the 3 main branches. Each region of the myocardium was connected to its closest arterial end branch, and all the subregions were identified as belonging to branches of either the LCA, RCA, or SpA (Fig. 3d_{i-ii}). The method estimated the LCA, RCA, and SpA to perfuse 60%, 25%, and 15% of the myocardium, respectively (Fig. 3d_{ii}). Using this information to tune outlet boundary conditions (Extended Data Fig. 4, Methods) resulted in close agreement between estimated perfusion territory and simulated flow splits (Fig. 3d_{iii}). Outlet boundary conditions were held constant as stenosis severity was increased. While this doesn't account for remodeling events due to the stenosis, we are specifically modeling the immediate flow of collaterals arteries that exist before a stenosis would develop. In total, the adjustments to the model and boundary conditions provided a model with close concordance to native physiology.

Our next goal was to investigate collateral blood flow, and one benefit of a computational approach is that parameters, such as collateral number/size and stenosis severity, can be virtually modified and systematically tested (Fig. 3e). We placed virtual collaterals within the native coronary tree model described above, using post-injury imaging data to guide general placement (see Fig. 3a). Computationally derived pressure values were then used to precisely adjust placement at each branch so that collaterals joined two regions of equal pressure. This minimized flow across collaterals without stenosis, which is important to establish a consistent baseline so that different configurations could be properly compared (Fig. 3e, Extended Data Fig. 5). These guidelines were used to produce 5 different collateral configurations in the adult heart (Extended Data Fig. 5). We compared pressure difference, flow, and shear stress in all collaterals from each configuration to Poiseuille's law, which analytically describes flow through a cylinder, to ensure our simulation results were reasonable (Extended Data Fig. 6, Methods).

The same workflow was performed for an uninjured P6 heart. Perfusion territories were similar, but a lower aortic inflow was prescribed for neonates to match published values[34,39]. Four collateral configurations were produced for neonates (Extended Data Fig. 5). Then, adult and neonate models were used to investigate re-perfusion upon virtual stenosis.

Investigating flow recovery by collateral arteries

One way to quantify re-perfusion is to sum the flows from all outlets downstream of the virtual stenosis and compare this to a normalized baseline flow with no stenosis (set at 100%). As expected, with no collaterals in adults total flow downstream of stenosis decreases when percent occlusion increases, especially above 90% (Fig. 4a, top row in chart). When comparing all the configurations tested at all stenosis levels, the configuration with 9 collaterals at 40 μm (9col, 40μm) provides the most flow recovery, especially at 99% stenosis where it restores almost 25% of the non-stenotic flow compared to just 1% without collaterals (Fig. 4a, right-most column in chart). However, this extent of collateralization does not occur naturally with coronary artery ligation in adult mice (see Fig. 2i and refs [7,8]). We noted that configurations similar to those observed experimentally, i.e. 6–12col, 20μm, recovered very little flow as measured by this method (Fig. 4a). These data demonstrate that

collateral arteries as they naturally form after adult coronary occlusion are not expected to appreciably recover blood flow, but that increasing diameters, which is a major factor in reducing overall resistance, could enhance their function.

In contrast, comparable collateral configurations in neonates performed well. The natural configuration (i.e. 12col, 20μm, see Fig. 2i and ref [7]) is estimated to recover up to 60% of total flow downstream of a 99% stenosis (Fig. 4b). Remarkably, the largest diameter tested (40 μm) only required one vessel to provide massive recovery (Fig. 4b, last row in chart). To compare adult and neonate flow recoveries, it is important to confirm that collaterals generally connect equal pressure zones (+/− 10 mmHg) so that all configurations start with a similar collateral flow. This was further evident by the observation that adding collaterals did not change total downstream flow without stenosis and primarily increased flow only with increasing stenosis severity (Extended Data Fig. 5).

The above analysis calculated overall recovery of pre-stenosis levels, but clinical data indicate that myocardial tissue could be supported at approximately 30% of baseline flow[40,41]. Thus, we next explored a more nuanced perspective by considering individual outlet perfusion territories downstream of the stenosis, so that we could observe if certain regions were receiving sustainable re-perfusion (i.e. >30% re-perfusion). First, we grouped all perfusion territories downstream of the stenosis to obtain the full volume-at-risk (Fig. 4c) and then plotted the percentage of that volume that is re-perfused above a certain threshold (Fig. $4c_i$). This revealed that while there were still no sustainably re-perfused regions in the 12col, 20μm and 6col, 28μm configurations, the 3col, 40μm and 9col, 40μm configurations were able to sustain 10 and 25% of the volume-at-risk, respectively (Fig. $4c_{i\text{-}iii}$). However, in the neonate, the 6col, 20μm re-perfused 80% of the volume-at-risk over the 30% threshold while the 12col, 20μm and 1col, 40μm configurations re-perfused the entire volume-at-risk (Fig. $4d_{i\text{-}iii}$). These data emphasized that collateral configurations of the same size, and thus same resistance, function better in the neonatal heart.

One hypothesis is that hemodynamic conditions at specific vessels dictate where collateral connections form. To gain evidence for this, we modeled an injured neonate heart 4 days after MI to identify if hemodynamic forces correlate with real collateral connection sites. 180 vessels of an injured neonatal heart were segmented (Extended Data Fig. 7ai). We then virtually removed the 9 injury-induced collaterals and fixed the occlusion to obtain a representative model of the coronary vasculature after the MI but before collaterals formed (Extended Data Fig. 7aii). Calculating pressures at tips near real collateral attachment sites and comparing those to non-attached tips in the injury region did not reveal a difference (Extended Data Fig. 7b). Comparing pressure at tips at the end of either the SpA (most common connection site) or RCA (least common connection site)(see Fig. 2h) in non-injured hearts also revealed no difference (Extended Data Fig. 7c). These data show a lack of correlation between hemodynamic factors and attachment site, suggesting that other factors, such as interaction with infarcted tissue (see Extended Data Fig. 3a and b), may play a more prominent role.

One interesting difference between the non-injured and injured models was that the volume perfused by the LCA was reduced due to vessel pruning downstream of the occlusion

(Extended Data Fig. 7aiii). Due to this pruning, the LCA had a large pressure drop even after the occlusion was relieved (Extended Data Fig. 7aiv). Consequently, after injury, there was a persistent pressure difference between the two connection sites (Extended Data Fig. 7d), which began to equalize once collaterals were added back into the model (Extended Data Fig. 7e). These observations suggest that real collaterals connect vessels of different pressure, and this difference is equalized towards a homeostatic level upon collateral connection.

Using the same neonate MI model, we next compared the performance of real post-MI collaterals to the virtual pre-MI vessels modeled in Figure 4. The real neonatal collaterals restored blood flow at slightly higher levels than predicted by our virtual scenario. Specifically, the 9 real collaterals with an average of 20μm were most similar to the 12 virtual collaterals at 20μm (Extended Data Fig. 7d and Fig. 4d_i, red dotted line). This was also true for volumes above 30% re-perfusion and total flow recovery (Extended Data Fig. 7e–f). This slight enhancement is likely due to the above describe vessel pruning causing a lower baseline flow being restored. In total, the similar magnitudes between real and virtual flow recoveries and volume re-perfusions support our predictions that neonatal collaterals have greater reperfusion abilities.

We next explored whether a more favorable placement of collaterals could improve the poor performance seen in adults. We started with a 3col, 40μm configuration (Fig. 5a, blue) and moved each collateral to a more proximal location in the coronary tree (Fig. 5a, red). This manipulation almost doubled total flow recovery (Fig. 5b) and approximately tripled the volume of myocardium re-perfused above the 30% threshold (Fig. 5c–e). Thus, variation in location can improve collateral function.

The above data suggested that fewer, larger collaterals are better than many, smaller ones (see Fig. 4). However, in those experiments, the total collateral resistance varied between the configurations. We tested this hypothesis by varying the number and size of the collaterals while keeping the total resistance equal. Simulations were performed on 2 configurations —16col, 20μm and 1col, 40μm (Fig. 5f). While total flow recovery was approximately equivalent (Fig. 5g), the 1col, 40μm configuration was uniquely able to re-perfuse 5% of the volume-at-risk above 30% (Fig. 5h–j). Streamlines from each collateral illustrate differences in flow distribution between the 16 collateral and 1 collateral configurations (Extended Data Fig. 8). This analysis shows that fewer, larger collaterals could be more beneficial because they at least protect a portion of the myocardium while many, smaller collaterals distribute the re-perfusion so that none reach protective levels.

Adult vs. neonate coronary artery morphology

Given that collaterals of the same size and total resistance were predicted to proportionally recover more flow in the neonate, we sought to understand why and first investigated arterial pressures at collateral formation sites. To facilitate comparisons, Strahler ordering was used to classify branch segments into orders based on hierarchal position in the coronary tree and vessel diameter[42,43]. Order 13 represented the aorta, order 12 represented the most proximal coronary artery segments, and subsequent orders represented downstream vessels until 8, which were the most distal branches modeled (Fig. 6a). This was used to compare

hemodynamic and anatomical quantities at similar points in the coronary tree in both the adult and neonate. While absolute aortic and proximal coronary (order 12) pressures were vastly increased in the adult, the pressures at the most distal coronary tips (order 8) were approximately equal (Fig. 6b and c). Quantification revealed that the pressure drop along the coronary tree was ~20 and ~50 mmHg in neonate and adults, respectively (Fig. 6c). This is also true when considering just the segments downstream of the stenosis, making $\Delta P_{Ad} > \Delta P_{Neo}$ (Fig. 6b and c). Thus, the collateral pressure difference (ΔP_{Col}) required to restore pre-stenotic flow downstream of the occlusion is higher in the adult. Specifically, the ΔP_{Col} needs to be about ~2-fold more in the adult to restore the same flow. Given that we see similar distal pressures at both stages, this explains why, even though collaterals in both recover the same absolute flow, it is much lower than the baseline, non-stenotic flow in the adult.

A sensitivity analysis was next performed to control for user variability in segmentation. We utilized 0D reduced order models (ROMs) due to the computational cost of running full 3D simulations. While 0D simulations do not account for pressure losses at junctions, perturbations of parameters in 0D models have been shown to be highly correlated with 3D perturbations[44]. The 0D ROMs were created by extracting radius, length, and connectivity of vessel segments using automated scripts and modeling the segments as simple resistors in a network[45] (see Methods). To quantify the expected variability of vessel segmentation, 5 users with knowledge of vascular anatomy determined the diameter of 16 segmentations sampled across all orders of the coronary tree. The average coefficient of variation was 16.7% (Extended Data Fig. 9a). We tested the extremes by decreasing the adult radius and increasing the neonate radius by 20%. This resulted in significant differences in ΔP_{Ad} and ΔP_{Neo}, demonstrating robustness of our overall findings (Extended Data Fig. 9b).

Our next experiments probed why ΔP_{Ad} was greater than $\Delta P_{Neo.}$ Two factors critical for determining ΔP are flow rate and total resistance. First, we compared the flow rate at each Strahler order between neonate and adult. Literature values indicated that aortic flow in adults is approximately ten times more than neonate, which was used as the inflow boundary condition for the computational model (see Fig. 3c)[34]. Simulations revealed that flow was also 10-fold greater for every vessel order modeled in the coronary tree (Fig. 6d). Shear stress was lower in neonates compared to adults, particularly in higher order vessels (Fig. 6e). We confirmed this trend held true when increasing the mesh size from 1.8 to 10 million elements; there was less than 10% difference in average shear stress with increased mesh resolution. Flow values were in line with increases in myocardial volume over time, i.e. volumes at P32 were more than 10-fold of P0 (Fig. 6f). We also observed a linear increase in myocardial volume during the first two weeks of life, a plateau between P18–25, and a burst of growth from P25–32. Second, we used the simulated flows and pressures to calculate the total resistance of the 3D coronary model. Neonate total vascular resistance was 3-fold that of adults (Fig. 6g). The neonate 3D coronary resistance is much higher due to significantly lower number of branches (quantified below). Since flow was increased by 10-fold, the 3-fold decrease in total resistance is not enough to offset flow increases. Thus, while the resistance of the coronary vasculature decreases in the adult, it is not able to lower the resistance enough to balance the much greater flow, manifesting in a greater ΔP in adults.

We next investigated what features contribute to the nonproportional decrease in resistance with respect to the flow increase from neonate to adult. Two factors critical for determining resistance are vessel diameter and number of branches. Increases in these parameters both work to lower total resistance, diameter being the most impactful. Surprisingly, we found that the diameters were the same across all Strahler orders in each model (Fig. 7a). We validated this by comparing diameters of the most proximal segments of the RCA, SpA, LCA and aorta in multiple replicates of neonatal and adult hearts (Fig. 7b). The coronary stem diameter remains virtually the same while aortic diameter increased with age (Fig. 7b), a result we validated using an orthogonal method (Fig. 7c). Thus, coronary diameters do not grow proportionally to heart volume, which suggests that diameter expansion does not function to relieve vascular resistance in the face of increased flow demand in adults.

If arteries do not increase in diameter, additional branches must be added to at least partially offset the increased flow that accompanies heart growth. We next quantified branching during postnatal development. Comparing the Strahler ordering of the two stages revealed that the number of distal vessels (order 9 and 8) were vastly increased (Fig. 7d), aligning with qualitative observations from imaging (see Fig. 1). Since the 3D SimVascular models did not contain arterioles distal to tertiary branches, we further investigated morphometry by manually tracing all α-SMA vessels in a representative branch—the Left Circumflex (LCx) (Fig. 7e, red). Imaris software filament tracing binned each segment of the LCx according to branching levels and quantified the number of arteriole tips (Fig. 7f). The number of branching levels spiked between P0–6 and then hit a plateau until another spike between P25–32 (Fig. 7g). Number of tips increased linearly up to P18 with another spike between P25–32 (Fig. 7h). To find a growth-halt point in adult mice, we quantified arterial tip numbers in two- and three-month-old mice, and found similar quantities to P32, suggesting a stop-point after one month of age (Fig. 7h). The P6–18 plateau in number of branch levels compared to the linear increase in number of tips over the same time period indicated that the coronary arteries grow by adding branch segments along the entire length of existing branches. We also observed that the length of each segment was constant among all ages tested (Fig 7i). This results in a coronary tree with many lateral branch segments of a set length.

Human fetal and adult coronary collateral arteries

A subset of human hearts contains collateral arteries, which are easily observed during an angiogram and are correlated with increased survival in heart disease patients[46,47]. We sought to identify how our computational modeling studies could help us better understand human collateral function. Thus, we compared the data available from human hearts to our mouse models. We measured vessel diameters for the collaterals observable in angiograms from five patients living with chronic total occlusions since these patients' collaterals can sufficiently support myocardial perfusion downstream of the occlusion without exercise (Fig. 8a). To compare to mouse data, we normalized human diameters to the most proximal segment of the LCA. Collateral diameters were on average 15 percent of the LCA (Supplementary Table 1). These values were in between those observed in the neonate and adult mouse hearts (Supplementary Table 1). Diameters in angiograms are measured in 2D projections affecting the accuracy of absolute values. We also found an average of

2 collaterals per heart (Supplementary Table 1), but comparisons with mouse data using this parameter are less desirable because angiograms will only highlight a subset of the collaterals that immunostaining would label. These data provide a foundation to determine re-perfusion benefit, but a very precise understanding in humans will need to consider the different pressure distributions resulting from human specific morphology.

Using post-mortem perfusions, studies from the 1960s reported the presence of coronary collateral arteries in infants and children[48,49], but no one has reported whether collaterals develop during embryogenesis. Furthermore, using smooth muscle coverage to identify collateral connections in humans has not been done. We processed two fetal hearts aged 17 and 22 weeks with the same whole-organ immunolabeling method used for murine hearts (Fig. 8b$_{i\text{-}ii}$ and Extended Data Fig. 10), imaged at high-resolution, and three additional hearts aged 14, 18 and 19 weeks, imaged at a lower resolution (Extended Data Fig. 10). Both, 17- and 22-week-old hearts had visible collaterals on the dorsal and ventral sides (Fig. 8b$_{iii\text{-}iv}$ and Extended Data Fig. 10). Remarkably, >17 collaterals were detected per side (Fig. 8c), which suggests that the whole human heart has at least 40 pre-existing, smooth muscle covered collaterals forming during (17–22 weeks) stages of embryonic development. On the ventral side, most connections bridged distal branches of the RCA and LCA while the majority on the dorsal side connected two LCA branches (Fig. 8d). Collateral diameters were not significantly different across locations or between ages and were on average 7 percent of the most proximal LCA segment (Fig. 8e). Thus, unlike mouse, human hearts have mechanisms in place to form native collateral arteries as part of normal development, evident by the numbers of collaterals in younger, 14 weeks age heart, less than half found in the older hearts (Extended Data Fig. 10d–f). We hypothesize these mechanisms could be the precursors for those that preserve myocardium downstream of an occlusion.

Discussion

This study applies 3D CFD to quantify hemodynamic forces in the adult and neonatal mouse coronary vasculature, the latter being naturally more restorative. The findings suggest the therapeutic benefit of promoting fewer, larger collaterals. Imaging the intact 3D arterial structure revealed its architectural complexity. Our methods also reveal a critical role for the SpA. Previous studies utilizing flattened hearts for whole-mount imaging failed to distinguish the SpA from the RCA[7]. Results point to SpA as a primary collateral connection site. The SpA proximal attachment configuration was proposed to impact cardiac recovery[50], and it will be important to assess the influence on collateral positioning. Collateral bridges preferentially formed within or near the infarct, further supporting local hypoxia as a trigger[7], but tissue stiffness or disrupted blood flow could also play a role.

Because there is no automated method to generate 3D artery models [23]. we manually segmented over 300 vessels in an adult and over 200 vessels in a neonate to ensure a high model fidelity for SimVascular fluid simulations. Methods for the brain utilize machine learning to improve automation (e.g. TubeMap)[51]. Future work will use or develop similar methods for cardiac vasculature.

One advantage of CFD modeling over *ex vivo* measurements of experimental samples is the capability to easily modify one feature, i.e. collateral structure, while keeping all other parameters constant. We tested multiple collateral configurations within the same model to understand the relationship of number, position, and diameter on flow recovery, without potential secondary effects from mouse-to-mouse variations in coronary structure. We considered flow recovery above 30% of non-stenotic perfusion levels as being beneficial because previous studies detected cardiac dysfunction when flow levels dipped below 25–30% of baseline[40,41]. Simulations demonstrated that increasing diameters or positioning collaterals more proximally restored more tissue to this 30% re-perfusion value, more than increasing numbers of smaller collaterals. Our data didn't determine the re-perfusion level required for cardiomyocyte viability, but did provide general guidelines of how parameters affect collateral flow and re-perfusion. Physical differences between phenotypes or conditions can be more confidently related to functional differences.

Surprisingly, the most effective collateral configuration modeled in the adult re-perfused only ~20% of myocardium above the 30% threshold. This aligns with consistent scar formation after permanent coronary ligation in mice[8] and underscores the importance of understanding blood flow through experimentally-induced collateral arteries when considering therapeutic implications. Conversely, virtual collaterals with the same characteristics re-perfused most of the myocardium in neonates. This, combined with more numerous and larger collaterals in neonates, likely contribute to their greater recovery post-MI[7].

We attributed the difference in collateral performance to a lower pressure drop in the neonatal coronaries because increased flows in adults are not compensated by equal reduction in vascular resistance. Our two models were segmented to a similar extent since artery tip pressure was approximately 40 mmHg at both ages. The more gradual, steady decrease in pressure in the adult arises from more extensive branching, similar to porcine coronaries[52]. We estimated a mild pressure drop in native neonate coronaries. However, the pressure downstream of the 3D model is expected to abruptly drop to capillary levels. The reduction in total coronary resistance from neonate to adult is in general concordance with μCT measurements of coronary vessels >40 μm, but our data is quantitatively much greater[30,53]. While these studies described the coronary tree with quantitative scaling laws, they were not able to quantify small diameter arteries, which were absent compared to our P6 hearts. Future work could investigate how quantitative scaling laws apply to vessels observed with organ clearing.

Since only a minority of adult human hearts have significant collateral flow, it was surprising that fetal hearts contained >40 native collaterals. Collaterals have been reported to decrease during adolescent years suggesting they may regress over time[48,49]. If we can preserve and enlarge these collaterals in adulthood, they may improve cardiac perfusion in patients suffering from CAD.

Overall, by combining advanced computational and imaging techniques, a critical connection between collateral flow, native morphology, and pressure distributions was established. By bridging these fields, we uncovered how fundamental coronary morphology

changes from embryonic to adult affect collateral flow. These findings provide insight into why coronary collateral arteries are better suited for recovering from injury in young hearts versus old.

Limitations

We did not measure subject-specific aortic flows and pressures for each mouse to generate boundary conditions, but instead used literature-derived averaged flows scaled to the model size. Our results are specific to LCA ligations and SpA-from-RCA coronary tree configurations. Virtual collaterals were assumed to be straight tubes while the tortuosity index of *in vivo* collaterals was on average 0.1 (±0.07), a small difference when compared to the much more tortuous human collaterals[54].

Due to small size and inaccessibility, coronary outlet pressures cannot be validated *in vivo*. Pressure measurements in rabbits and dogs show 50–70% pressure loss at the capillary bed[55,56]. Our outlet boundary conditions were 65% of the total coronary resistance to match literature values[55]. We changed outlet pressure by adjusting the outlet resistances and found relative differences between the collateral configurations remained the same.

Our modeling does not account for short or long-term effects of vasodilation or remodeling. Adult coronaries compensate for ischemia through autoregulatory vasodilation. Recent studies have accounted for autoregulation, enabling accurate predictions of fractional flow reserve[57–59]. However, autoregulatory effects remain uncharacterized in neonatal hearts. Once quantified *in vivo*, they could be incorporated into future modeling approaches. If autoregulatory effects are similar in adult and neonate, our conclusions on the relative differences in collateral performance are expected to remain unchanged. Vascular pruning and scar development following adult injury could impact downstream resistance, but requires *in vivo* experiments to obtain mouse-specific modeling parameters. Future studies will enhance our computational methods by using *in vivo* experiments to define and capture autoregulation and remodeling.

Methods

Animals

All mouse colonies were housed and bred in the animal facility at Stanford University in accordance with institutional animal care and use committee (IACUC) guidance on 12 h/12 h day and night cycle with water and food ad libitum.

The following mouse strains were used: pure C57BL/6J, (Jackson Laboratory, strain code: 000664) pure CD1 (Charles River, strain code: 022) and mixed C5BL6 & CD1. Both male and female mice were used for postnatal studies up to day 6. Males were exclusively used for studies of postnatal day 11 to 3mo.

All experiments were conducted in accordance with protocols approved by the Institutional Animal Care and Use (IACUC) Committee of Stanford University.

Immunolabeling and iDISCO clearing

Whole heart vasculature staining was performed following the modified iDISCO+ protocol previously described[12,28]. For all following steps, tissue was always agitated unless noted otherwise. Briefly, animals were perfused with PBS through the dorsal vein, and fixed in 4% paraformaldehyde (Electron Microscopy Science 15714) at 4°C for 1hr (neonatal hearts) or 2hr (adult hearts), washed 3X in PBS and stored in PBS with 0.01% sodium azide (w/v, Sigma-Aldrich S8032) until ready to process. Hearts were dehydrated in increasing series of methanol/ddH_2O dilutions (20%, 40%, 60%, 80%,100% 2X) for 1hr each, followed by overnight incubation in 66% dichloromethane (DCM, Sigma-Aldrich 34856) and 33% methanol. Next, tissue was washed 2X in methanol 100% for 4hrs and bleached overnight at 4°C in 5% hydrogen peroxide (Sigma-Aldrich 216763) in methanol. Next, the hearts are rehydrated in methanol/ddH_2O dilutions (80%, 60%, 40%, 20%) for 1hr each, followed by PBS, 0.2% Triton X-100 PBS (2X) and overnight 20% dimethyl sulfoxide (DMSO), 2.3% Glycine (w/v, Sigma G7126), 0.2% Triton X-100 PBS at 37°C for 2 days. For immunostaining, hearts were blocked in 10% DMSO, 6% Normal Donkey Serum (NDS, Jackson ImmunoResearch 017-000-121) in 0.2% Triton X-100 for 2 days at 37C. Primary antibodies, αSMA-Cy3 conjugated (1:300, Sigma C6198), Connexin-40 (1:300, Alpha diagnostic cx40A), and Podocalyxin (1:1000, R&D Systems MAB1556) were prepared in PBS with 5%DMSO, 3% NDS in 0.2% Tween-20, 0.1% Heparin (w/v, Sigma-Aldrich H3393) and incubated at 37°C for 4–14 days. Secondary antibodies conjugated to Alexa 647 (Jackson ImmunoResearch) were matched 1:1 in concentration to their primary target and in prepared in PBS with 3% NDS in 0.2% Tween-20, 0.1% Heparin for the same primary incubation days at 37°C. Washes after each antibody incubation in PBS with 0.2% Tween-20, 0.1% Heparin were performed in 30min increment until the end of the day, followed by an overnight wash. Before clearing, samples were embedded in 1% low-melting agarose (Sigma-Aldrich A9414) in PBS and dehydrated in methanol/ddH_2O dilutions (20%, 40%, 60%, 80%,100% 2X) for 1hr each and 100% overnight. Next, hearts were incubated in 66% DCM and 33% Methanol for 2.5hrs, followed 2X 30min 100% DCM. Finally, samples were cleared in ethyl cinnamate (ECi, Sigma Aldrich 112372), manually inverted a few times, and kept at RT in the dark until and after imaging.

Light sheet imaging

Samples were imaged with Imspector Pro 7.0.98 software and LaVision BioTec Ultramicroscope II Light sheet microscope in a quartz cuvette filled with ECi. For imaging, we used a MVX10 zoom body (Olympus) with a 2x objective (pixel size of 3.25 μm / x,y) at magnification from 0.63x up to 1.6x. Up to 1400 images were taken for each heart and the z-steps are set to 3.5μm z step size, and light sheet numerical aperture to 0.111 NA. Band-pass emission filters (mean nm / spread) were used, depending on the excited fluorophores: 525/50 for autofluorescence; 595/40 for Cy3; 680/30 for AF647 and 835/70 for AF790. Exposure time was 10ms for single channel and 25ms for multichannel acquisition.

Perfusion territory mapping

To determine the approximate volume of myocardium each outlet of the coronary model was responsible for perfusing we used (1) a model of the myocardial tissue as the total volume

to be perfused and (2) the outlet coordinates as the seed points for the subvolumes. We used the background signal from the staining to segment the model of the myocardial tissue and the cap centers for the outlet coordinates. Then, we used a Voronoi diagram algorithm to assign subvolumes of the myocardial tissue to each outlet of the coronary model such that every point in the myocardial mesh was assigned to the closest outlet. Distances to the closest outlet were determined using a dijkstra algorithm. By integrating the subvolumes of every outlet on each of the 3 main branches (LCA, RCA, and SpA), we were able to calculate the approximate percentage of the total myocardial volume that each main branch is responsible for. We used these percentages as targets for the flow splits when tuning the outflow boundary conditions for the fluid simulations.

We used outlet coordinates instead of centerlines because we were able to better resolve the small coronary arterioles compared to prior studies[60]. This allows us to be certain that myocardial regions close to an outlet are perfused by that outlet, rather than by a large artery nearby that has no outlet nearby.

CFD simulation

We constructed 3D subject-specific models of the mouse vasculature using SimVascular (2021.06) cardiovascular modeling pipeline[33]. Briefly, we created path lines for each vessel (about 349 vessels for the adult and 244 for the neonate). Vessels distal to the quaternary branches were ignored. For each path line, the image data was viewed in planes orthogonal to the tangent of the path line to segment the cross-section. Circles were used to approximate the cross-section, as some areas of the vasculature appeared collapsed or deformed. All segmentations were lofted to create a solid model of each branch, and the branches were then unioned together to form a complete geometric model. Finally, the lofted model was discretized into a linear tetrahedral mesh using the commercial meshing library, MeshSim (Simmetrix, Troy, NY), resulting in a total of 600 thousand and 1.8 million elements for the neonatal and adult models, respectively.

After obtaining the mesh, we uniformly scaled it to account for the shrinkage that occurs via iDISCO. We quantified the volume change due to our specific clearing protocol using water displacement pre- and post- iDISCO and found that the heart shrank to about 63% of its original volume. So, we uniformly scaled the entire volumetric mesh by the inverse (1.58-fold) to ensure that our model faithfully matched the pre-iDISCO geometry (equation 1).

$$V_{post} = \frac{1}{.63} V_{pre} = 1.58 V_{pre} \quad (1)$$

Inlet boundary conditions were determined as follows. We first determined typical neonate and adult mean pressure and aortic velocity values from literature[34,35,61] (Supplementary Table 2, rows 1–2). Using the mean aortic velocity and the aortic cross sectional inlet area for each mouse used, a subject-specific aortic inflow was calculated and applied. For pulsatile flow simulations, we constructed representative flow waveforms for an adult mouse by digitizing, smoothing, and scaling a waveform from the literature to match the

mean inflow at both ages as calculated previously[62]. At the aortic outlet, we applied a simple RCR boundary condition[36] (Supplementary Table 2, rows 3–5). At the coronary artery outlets, we applied a specialized lumped parameter network (LPN) to represent the downstream coronary vasculature and the time-varying intramyocardial pressure due to the beating cardiac tissue[37,38,63] (Supplementary Table 2, rows 6–10). The resistance of each coronary outlet was estimated using Murray's law and tuned such that each of the 3 main branches (LCA, RCA, and SpA) had flow splits equal to the percent volume they perfused. We further tuned the capacitances and resistances of the coronary outlet boundary conditions to match literature values of the proximal and distal resistance ratio[55,56]. To do this, we used a 0D surrogate model for increased efficiency (Extended Data Fig. 2).

We globally corrected the viscosity in our pulsatile simulations to 1.25cP to account for the Fahraeus-Lindqvist effect; this is necessary because the apparent viscosity of blood decreases in very small tube diameters (<100μm)[64]. While this may significantly underestimate the shear stress in the aorta, the pressure drop in the coronaries was more representative and important for the findings presented here (see Limitations).

We ran blood flow simulations with rigid walls using the stabilized finite element svSolver code in the open-source SimVascular software package[33] to determine spatially and temporally resolved hemodynamic values, such as pressure, velocity, and wall shear stress at every node in the computational mesh. Simulations ran for 5 cardiac cycles with timesteps of .0001 seconds, and hemodynamic values were determined based on the final cardiac cycle. Flow and pressure waveforms converge to time-periodic solutions with less than 5% difference from cycle 5 to 6. Simulation time was approximately 40 hours on 96 cores via XSEDE and 90 hours on 96 cores via Sherlock. Paraview 5.9.1 software was used for visualization of the results.

Virtual collateral placement

Virtual collaterals were strategically added to native coronary vasculature to minimize the initial pressure difference of the two points the collateral was connecting. Specifically, based on an initial simulation of the native vasculature (without any virtual collaterals), a pressure distribution was determined. Using this pressure distribution, virtual collaterals were placed such that each connected equal pressure zones. We replicated realistic connections as closely as possible given upstream native vessel diameter and pressure constraints (Extended Data Fig. 3). The resistance of each collateral configuration was calculated via Poiseuille's Law (equation 2).

$$Total\ Collateral\ Resistance = \frac{8\mu L}{\pi n r^4} \tag{2}$$

Where μ is the viscosity, L is length of the collateral, n is the number of collaterals in the configuration, and r is the radius of the collateral.

3D Resistance

To calculate the resistance of the 3D model, we first generated vessel centerlines via the Vascular Modeling Tool Kit (VMTK; vmtk.org). Each point in the centerline was identified as a branch segment if a perpendicular cross-section at that point did not intersect with any other centerline point. If the cross-section intersected more than one centerline point, then it was labeled as a junction region. This separated the centerline into junctions and branch segments between junctions. After labeling every point, we determined the parent (upstream) branch segment and child (downstream) branch segments for each junction region. We then calculated the resistance for each branch segment based on the pressure difference from the most proximal to distal point and the flow within that segment from the simulation. Finally, the overall 3D resistance was calculated starting from the most distal branches using a recursive method to add the segment resistances in parallel or in series based on the connectivity.

Diameter-defined Strahler Ordering

We utilized the diameter-defined Strahler ordering system to compare morphometric and hemodynamic quantities at similar positions in the coronary tree between the neonate and adult. This system has been used in previous morphometric studies to classify branch segments into orders that describe the hierarchical nature of a vascular tree[42,65,66]. Using the same labels for branch segments and junction regions as in the 3D resistance calculations, we determined the initial Strahler ordering by setting the most distal segments to order 1 and working backwards up the coronary tree to the aorta. Parent segment orders were set to either equal the greater child order if the two children orders were different or incremented by one if the two child orders were the same. Since neither 3D model of the mouse vasculature included all arteries down to the capillary level (only 5 distinct orders here vs. 11 in other studies[43]), we translated all the orders by a constant such that the order of the most proximal segment of the coronaries was 12 and the aorta was order 13 to ensure consistency with previous studies. Segments were then re-organized based on their diameter to ensure that unbalanced branching (i.e. a very small vessel branching from a large one) was properly accounted for. To do this, we iteratively moved segments to higher or lower orders such that every segment within an order was within 1 standard deviation of that order's mean diameter. With the final diameter-defined Strahler ordering, we compared quantities such as diameter, length, flow, and pressure between the same orders of the neonate and the adult.

User study of diameter variability

To measure the human source of uncertainty in vessel diameter, we asked 5 users to segment the same 16 locations along 3 different vessels. These segmentations were sampled from both proximal, large and distal, small vessels. The users had extensive knowledge of vascular anatomy and were given the same instructions of how to segment the vessels using SimVascular. The coefficient of variation was measured for each segmentation and averaged to use for sensitivity analysis.

0D simulation and sensitivity analysis

We extracted radius, length, and connectivity information from centerlines generated through VMTK from the neonate and adult coronary tree (see 3D resistance) to create an input file for 0D simulation. Any modification of the radius for sensitivity analysis was directly scaled in the input file of the simulation. We ran 0D simulations using the svzerodsolver code in the SimVascular software package as previously described[45]. Each arterial segment was modeled as a resistor with a resistance value following Poiseuille's Law. The resistors were connected in parallel at each junction depending on the connectivity of coronary network. The input and output boundary conditions were the same as 3D simulations: a pulsatile waveform at the inlet, a RCR boundary condition at the aortic outlet, and coronary LPN at coronary outlets. Simulations ran for 10 cardiac cycles with timesteps of 0.001 seconds taking approximately 20 seconds of computational time.

Semi-automated artery tracing

Subsequential images were imported into NIH Fiji ImageJ 1.53 software as stacks files, these stacks were then converted into 8-bit and resolution reduced to one-fourth the original. Using ImageJ's plug-in, Simple Neurite Tracer, the branch structures of the LCx were able to be drawn by placing seed points along the length of α-SMA+ vessels[32]. Once every α-SMA+ artery in the LCx branch was completely accounted for within the trace, isolation of the traces was performed by the Fill Out option within the plug-in. The resulting image stack was used as a 3D outline of the arterial structure as the foundation for further modeling and analysis. After discontinuation of Simple Neurite Tracer, the updated version SNT was used in similar manner as above[31]. Quantitative metrics from tracing were similar between 4 independent researchers.

Tortuosity index quantification

Tortuosity index of collaterals was defined as follows, (equation 3)

$$tortuosity = \frac{L}{L_0} - 1 \tag{3}$$

where L is the total length along the centerline of the collateral and L_0 is the distance between the start and end of the collateral.

3D Rendering

The non-traced image stack was overlaid with the filled LCx stack using the Add Channel option in Imaris 9.5.0 software (Bitplane). Pixel dimensions were updated from the non-reduced 16-bit image metadata. The Filament Object Tracer module was used to generate an Imaris customizable 3D LCx branch model. Branch tips and length were measured by automatically generated data under Number of Terminal Points, and Total Length fields, respectively. Branch levels were obtained from the Filaments Branch Hierarchy field.

Surface objects in Imaris were used for quantifying the sample heart volumes. Myocardium volume was calculated by creating surface objects surrounding the entire sample surface and

objects encompassing the lumen of the ventricles. The volumes of the ventricles were then subtracted from the entire heart volume to result in the myocardium tissue volume.

Murine LCA ligations

Neonatal LCA ligations were performed as previously described[7] with minimal modifications. P2 neonates were cooled on ice for 6 minutes to induce hypothermic circulatory arrest and placed in a supine position followed by disinfecting with iodine and ethanol. Dissection was carried through the pectoralis major and minor muscles, and the thoracic cavity was entered via the 4th intercostal space. The LCA was identified and ligated at with a doble knot using 8–0 nylon suture, leaving the LCx intact. The chest muscle and skin were then closed (independently) with interrupted 7–0 prolene sutures. The neonate was then allowed to recover at 37°C warm plate and, when conscious, returned to its mother's care.

Adult mice were performed as previously described[67]. Adult mice were subjected to permanent coronary artery ligation, under anesthesia using initially 1.5%–4% isoflurane chamber for induction. The chest cavity was opened, and a 7–0 silk suture was placed around the left coronary artery, with occlusion verified by blanching of the underlying myocardium. The chest was then sutured closed. Following surgery, Buprenorphine (0.1 mg/kg) was used as an analgesic.

In vivo CD31 labeling

Neonates 4-days post-MI were cooled on ice for 6 minutes to induce hypothermic circulatory arrest and placed in a supine position. Mice received an intravenous 10 μl retro-orbital injection[68] of rat anti-mouse CD31 AlexaFluor 647 in sterile 1X PBS (1:5, BioLegend, 102516). Neonates were then allowed to recover at 37°C warm plate and, when conscious, returned to their mother's care for 30min before sacrifice.

Immunohistochemistry and confocal microscopy

Neonatal or adult hearts were fixed in 4% PFA overnight at 4 °C, and then cryopreserved in 30% sucrose in PBS for 1 day at 4°C. The following day, coronal heart sections (50 μm in thickness) were cut on a cryostat. Sections were rinsed 3X with PBS, blocked in 5% NDS, 0.5% Triton X-100 in PBS for 1hr at RT, and then incubated with αSMA-Cy3 conjugated (1:300, Sigma C6198) in 0.5% Triton X-100 in PBS overnight at 4°C. Next, sections were rinsed 3X in 0.5% Triton X-100 in PBS and then mounted on slides and covered with Fluoromount G (SouthernBiotech 0100-01). Tissue was imaged using inverted Zeiss LSM-700 confocal microscope at 5x objective. Digital images were captured with Zeiss Zen 2.3 software and measured using ImageJ.

Human hearts

Under IRB approved protocols, human fetal hearts were obtained for developmental analysis[69]. Gestational age was determined by standard dating criteria by last menstrual period and ultrasound[70]. Tissue was processed within 1hr following procedure. Tissue was extensively rinsed with cold, sterile PBS while placed on ice, followed by incubation in

sterile 4% PFA for 4hrs at 4°C before further iDISCO processing. Pregnancies complicated by multiple gestations and known fetal or chromosomal anomalies were excluded.

Human adult samples were acquired from the Stanford Catheterization Angiography Laboratory. All patients displayed symptoms of chronic angina and were scheduled to receive conventional coronary angiography, which was performed according to local clinical standards. Collateral number and size were confirmed by an experienced cardiologist. All patients were consented under an approved IRB protocol at Stanford University.

Statistical Analysis

Graphs represent mean values obtained from multiple experiments and error bars represent standard deviation. Two-tailed unpaired Student's t test was used to compare groups within an experiment and the level of significance were assigned to statistics in accordance with their p values (0.05 flagged as ∗, 0.01 flagged as ∗∗, less than 0.001 flagged as ∗∗∗, less than 0.0001 flagged as ∗∗∗∗). All graphs were generated using GraphPad Prism 9.1 software. Error bars represent ± standard deviation.

Extended Data

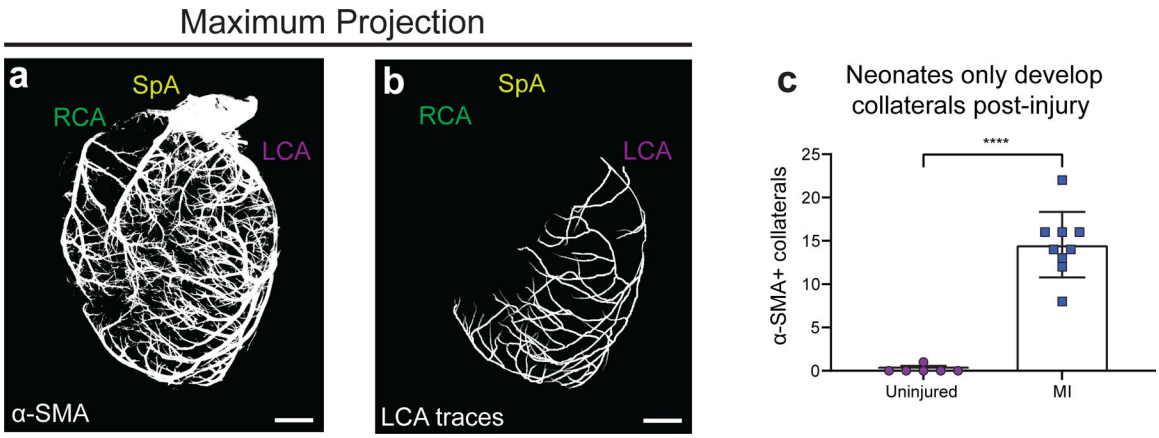

Extended Data Figure 1. Collateral formation in neonatal mice is a response of injury.
(**a**) Maximum intensity projections of a representative, non-injured neonatal P6 heart immunolabeled with α-SMA. (**b**) Maximum projection of traces beginning at the most proximal segment of the left coronary artery (LCA) and extended until the α-SMA signal discontinues. (**c**) Quantification of collateral numbers in healthy and injured (4-days post MI) neonatal hearts. n=6 uninjured, n=9 injured hearts. Scale bars, 500 μm. Error bars are mean ± st dev: ****, p≤.0001 by two-sided Student's t-test.

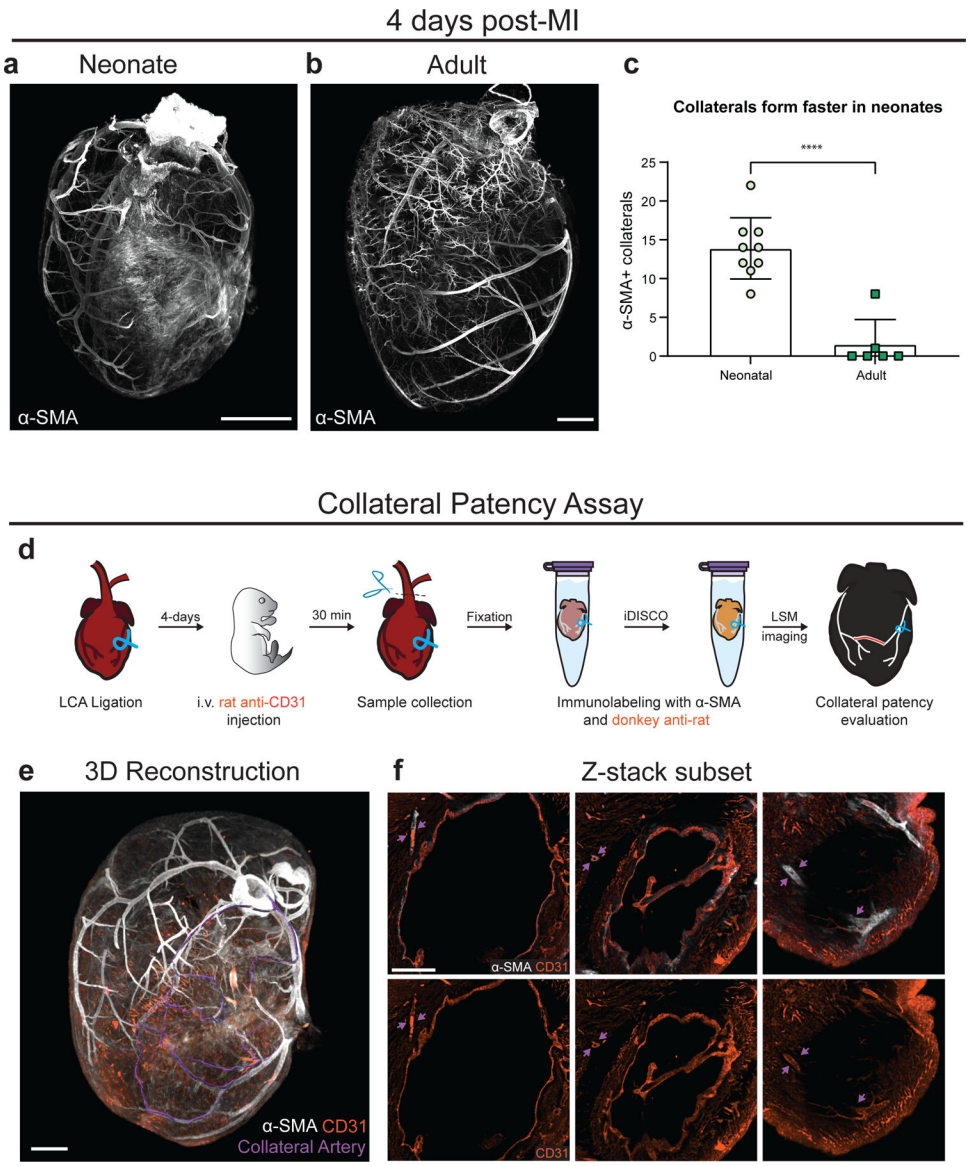

Extended Data Figure 2. Collateral artery assessments.

(**a-b**) Maximum intensity projection of an entire neonate and adult heart 4-days post myocardial infarction (MI) immunolabeled with α-SMA. (**a**) P6 neonatal heart. (**b**) Adult (12-week-old) heart. (**c**) Collateral numbers in neonate (n=9 hearts) and adult (n=6 hearts) 4 days post-MI. (**d-f**) Evaluation of collateral patency in P6 neonatal heart 4-days post MI. (**d**) Schematic of staining method. (**e**) 3D reconstruction of α-SMA+ collaterals (purple) overlaid with α-SMA and CD31 staining. (**f**) MIPs of representative Z-stacks (30 μm) within **e** highlighting (solid purple arrow) a patent (α-SMA+ and CD31+) collateral. Scale bars: **a** and **b** 1 mm; **e** 500 μm. Error bars are mean ± st dev: ****, p≤.0001 by two-sided Student's t-test.

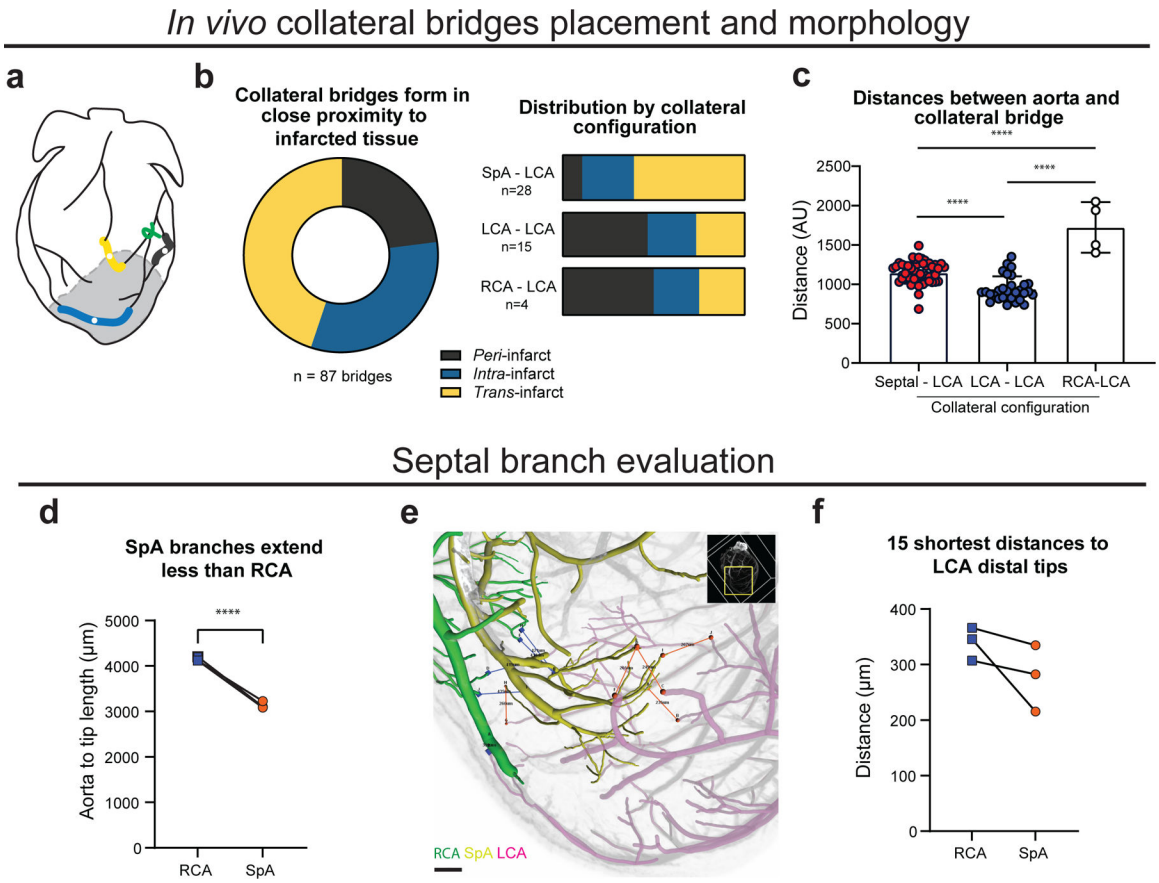

Extended Data Figure 3. Investigation into parameters related to collateral artery placement.

(**a-b**) Location of collateral bridges in relationship to infarcted tissue. (**a**) Schematic of categorization shown in **b**. (**b**) Pie chart showing distribution of collateral location (n=87 collaterals, n=6 hearts). Distribution by collateral configuration type (n=47 collaterals, n=3 hearts). (**c**) Distances between the aorta and collateral bridges (n=47 collaterals, n=3 hearts). (**d-f**) Septal artery evaluation. (**d**) Distances between most distal RCA and SpA branch tips to the aorta. (**e**) Representative image of 3D rendered coronary artery branch tips and distances. (**f**) Quantification of distances in **e** between most distal branch tips of RCA and SpA to LCA. Right (RCA), left (LCA), and septal (SpA) coronary arteries. **d-f,** n=3 hearts. Error bars are mean ± st dev: ****, p≤.0001 by two-sided Student's t-test.

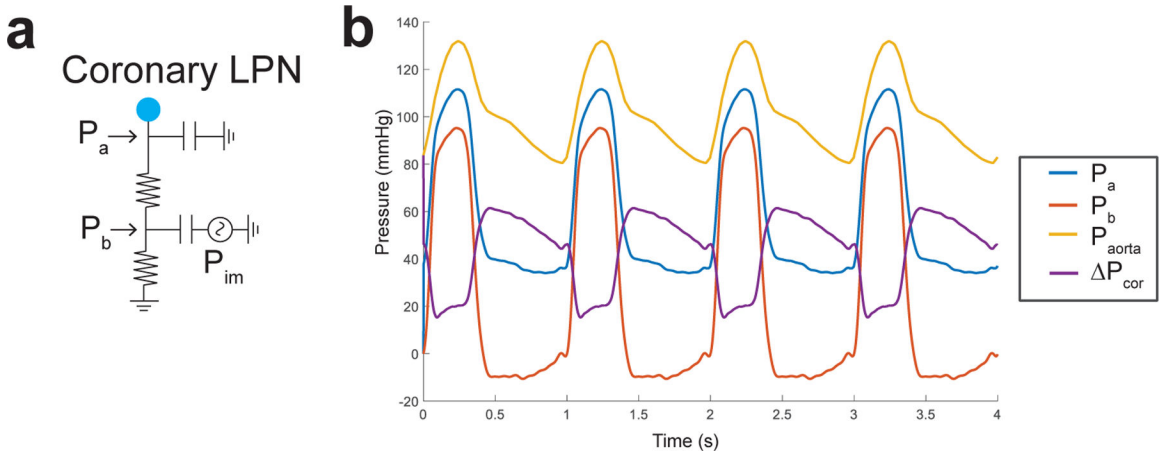

Extended Data Figure 4. 0D surrogate model of pulsatile coronary flow.

(**a**) Schematic of coronary lumped parameter network (LPN). (**b**) Pressure quantities of the coronary LPN. P_a, Pressure at point a; P_b, pressure at point b; P_{aorta}, pressure at aortic inlet; ΔP_{cor}, pressure difference between P_{aorta} and P_b.

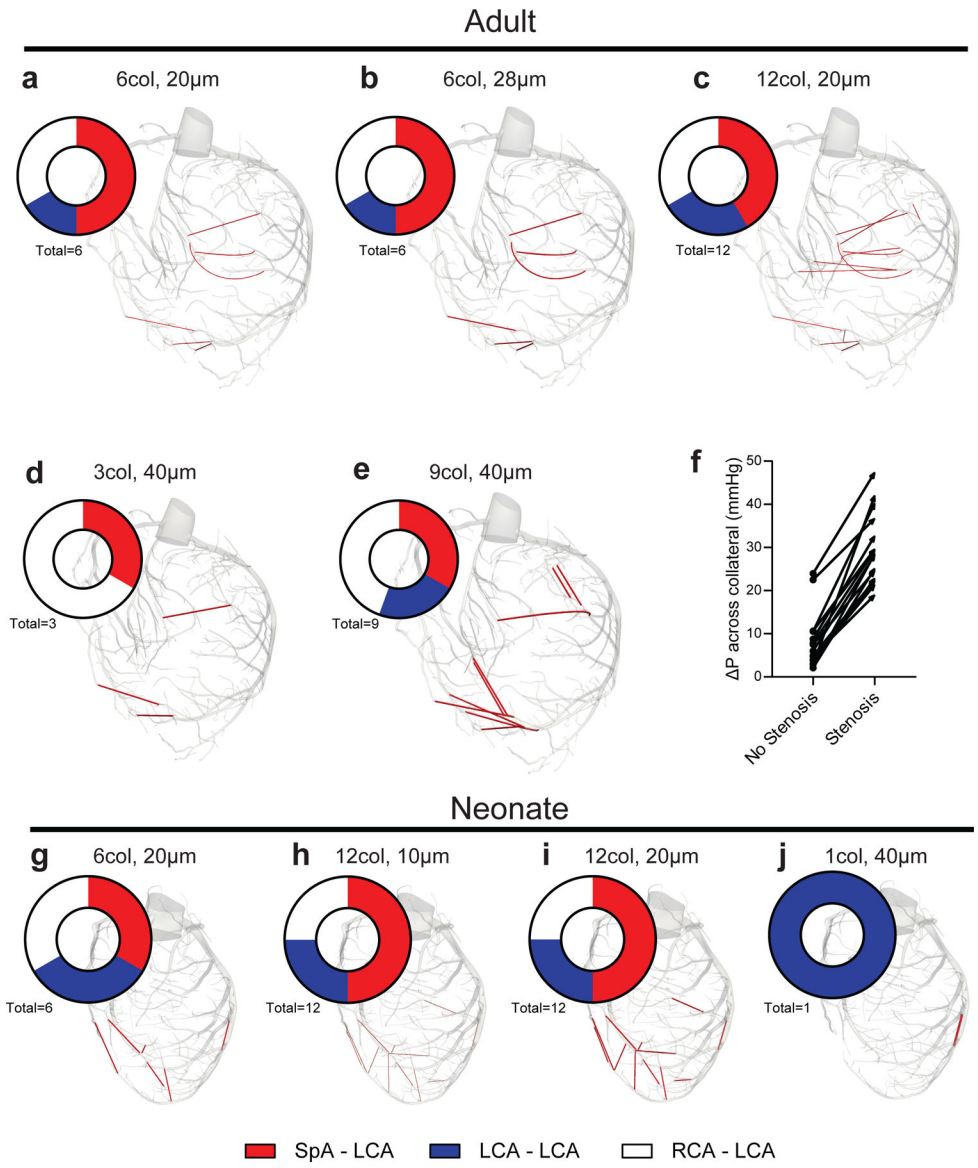

Extended Data Figure 5. Virtual coronary collateral configurations in adult and neonates.

(**a-e**) Adult configurations: 6 collaterals, 20 µm (**a**); 6 collaterals, 28 µm (**b**); 12 collaterals, 20 µm (**c**); 3 collaterals, 40 µm(**d**); 9 collaterals, 40 µm (**e**). (**f**) Pressure increases for each collateral in **c** with and without a 99% stenosis. (**g-j**) Neonatal configurations: 6 collaterals, 20 µm (**g**); 12 collaterals, 10 µm (**h**); 12 collaterals, 20 µm (**i**); 1 collateral, 40 µm (**j**). Pie chart indicates number of collaterals per connection type.

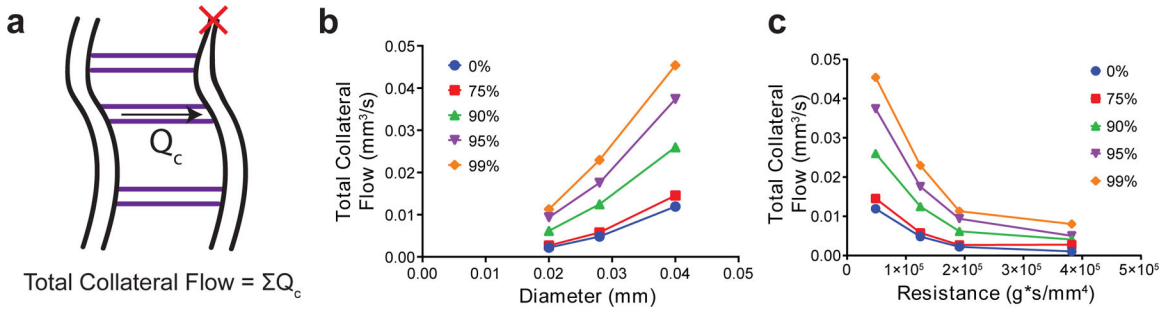

Extended Data Figure 6. Verification that collateral flows are in line with expected solutions.

(**a**) Schematic of total collateral flow quantification. (**b**) Total collateral flow vs. diameter of the collateral at each stenosis level. (**c**) Total collateral flow vs. resistance of the collateral configurations 6 collaterals, 20 μm; 12 collaterals, 20 μm; 6 collaterals, 28 μm; 3 collaterals, 40 μm. Resistance was calculated based on the number, diameter, and length of the collaterals via Poiseuille's Law.

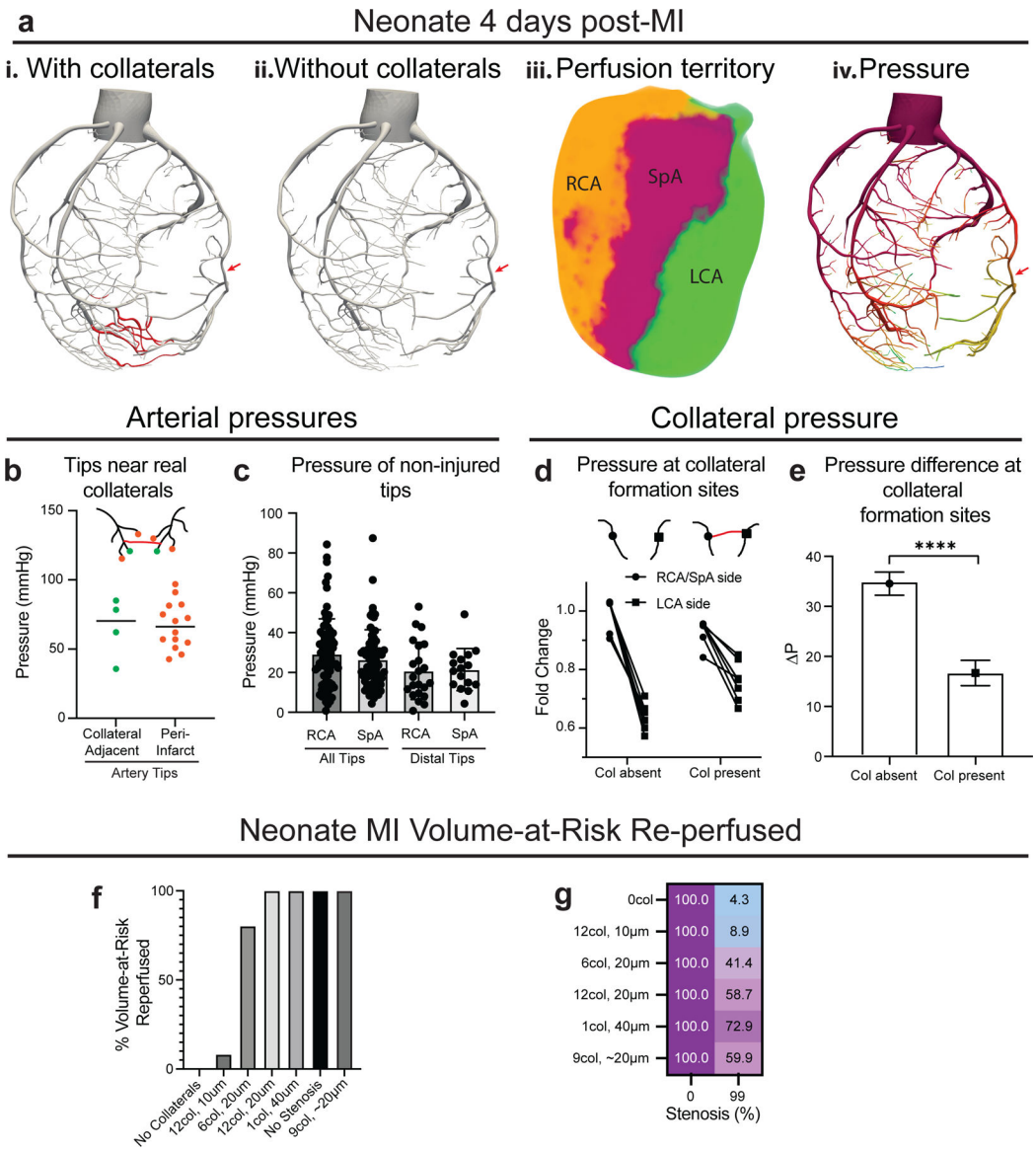

Extended Data Figure 7. Performance of neonate collaterals formed 4 days post injury.

(**a_{i-ii}**) Coronary vasculature with (**a_i**) and without (**a_{ii}**) collaterals formed in response to injury, respectively. (**a_{iii}**) Perfusion territories of the left (LCA), right (RCA), and septal (SpA) coronary arteries. (**a_{iv}**) Pressure distribution based on CFD simulation. Red arrow indicates location of occlusion that has been virtually restored. (**b**) Pressures at tips near real collateral (red segment) attachment sites (green circles) after injury and non-attached tips (orange circles) in the injury region. (**c**) Pressure at every tip and only distal tips of the SpA or RCA in non-injured hearts (n=81 all RCA tips, n=67 all SpA tips, n=22 distal RCA tips, n=16 distal SpA tips, n=1 heart). (**d**) Fold change at the connection sites of the collateral (red segment) when it is present and removed. The circle on the left is the pressure on either the RCA or SpA branch and the square on the right is the pressure on the LCA branch. (**e**) The difference in pressure across the two connection sites with and without the collateral (n=8 connections, n=1 heart). (**f-g**) The bar graph of percent volume-at-risk (VaR) above

30% (**f**), and total flow in vessels downstream of the virtual occlusion (**g**) within the VaR. Error bars are mean ± st dev: ****, p≤.0001.

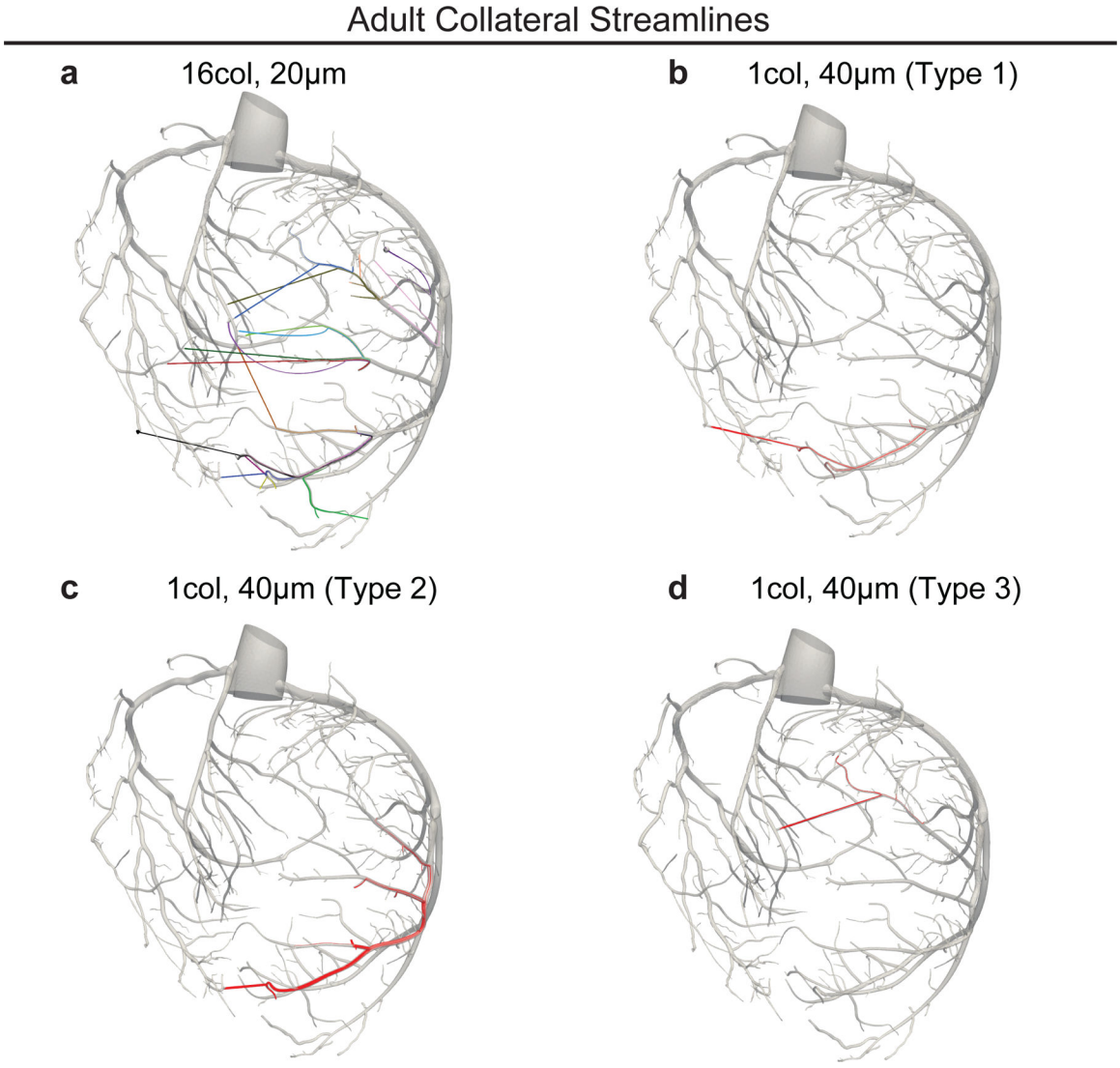

Extended Data Figure 8. Streamlines of adult collaterals.

(**a-d**) Streamlines of collateral flow for configurations: 16 collaterals, 20 μm (**a**) and 3 different types of 1 collateral, 40 μm (**b-d**). Colors represent the streamlines from 1 collateral.

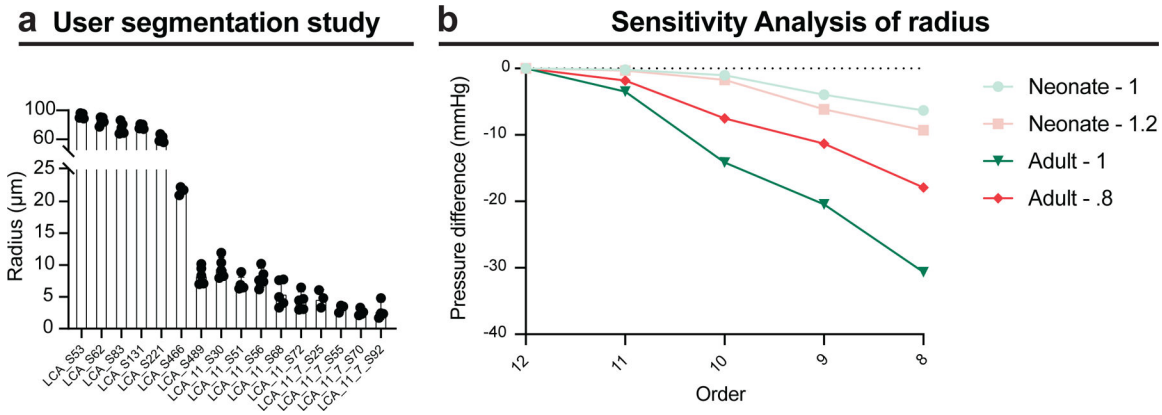

Extended Data Figure 9. User segmentation variability and sensitivity analysis.

(**a**) Radius measurements from 5 users of 16 segmentations over 3 vessels. The coefficient of variation is 16.7%. (**b**) Sensitivity of pressure drop along the coronary tree to the radius of segmented vessels. Adult vessel radius was reduced by 20% and neonate vessel radius was increased by 20%.

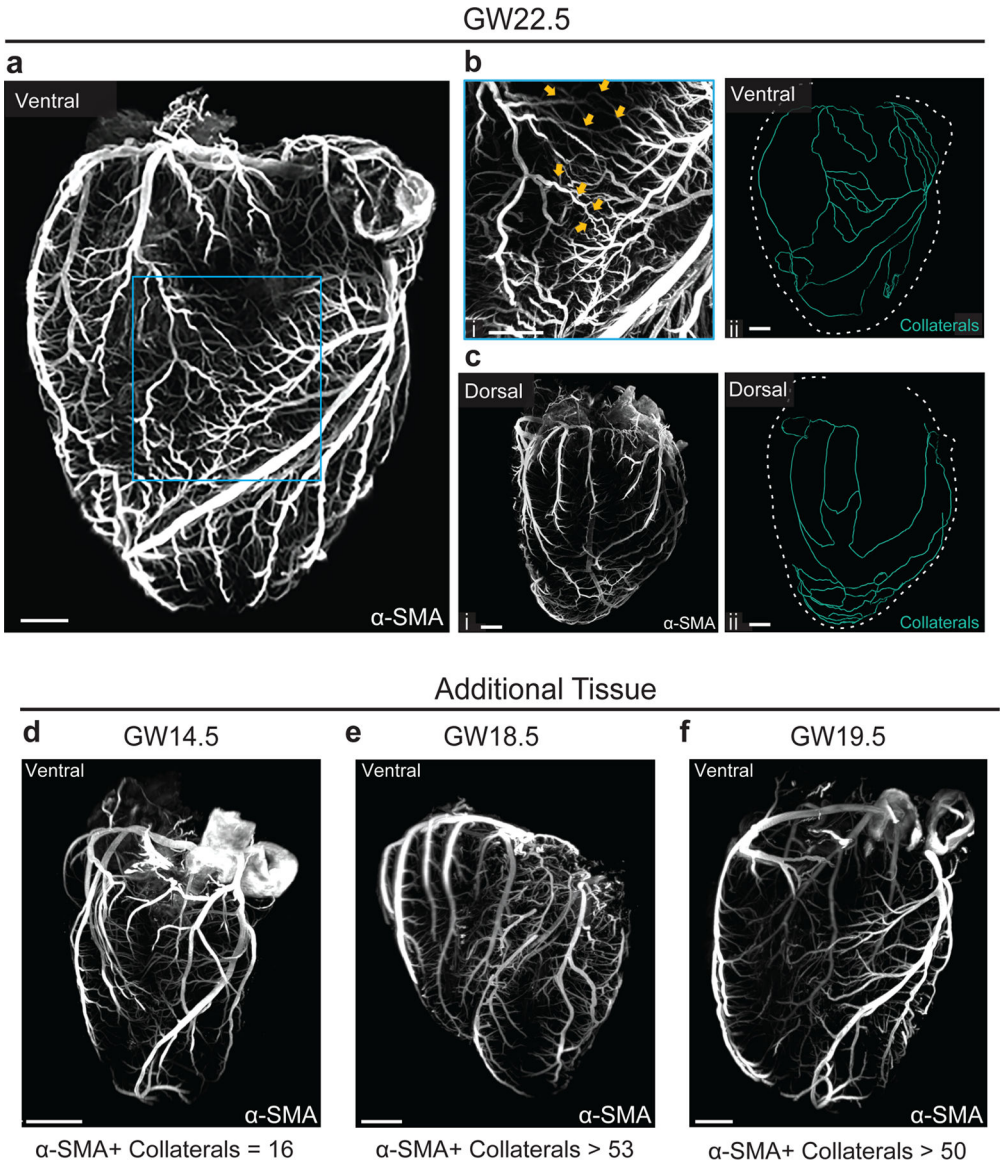

Extended Data Figure 10. Collaterals in fetal human hearts.

(**a**) Maximum intensity projection (MIP) of GW22 fetal human heart labeled with α-SMA, ventral side. (**b_i**) ROI of ventral side (blue boxed region). Closed orange arrows point to collateral segments. (**b_{ii}**) Traced collateral connection (green filaments) on ventral side. (**c_i**) MIP of fetal human heart, dorsal side. (**c_{ii}**) Traced collateral connections (green filaments) on dorsal side. (**d-f**) MIP of entire fetal human GW14.5 (**d**), GW18.5 (**e**) and GW19.5 (**f**) hearts, ventral side. Scale bars, **a-f**, 1.5 mm.

Supplementary Material

Refer to Web version on PubMed Central for supplementary material.

Acknowledgements

We thank Andrew Olson and Marco Howard for technical support of Light sheet imaging, and Hanjay Wang for advice on surgical procedures. S.A is supported by BioX Bowes Fellowship. P.E.R.C is supported by the NIGMS of the National Institutes of Health (NIH T32GM007276) and NSF-GRFP (DGE-1656518). M.L.D is supported by the NSF-GRFP (DGE-1656518). D.B. is supported by the Department of Defense CMDRP in Congenital Heart Disease (W81XWH-16-1-0727). K.N. is supported by the NIH/NHLBL (R01HL141712; R01HL146754). A.L.M is supported by NIH (R01EB018302) and NSF Award (1663671). K.R.H. is supported by the NIH/NHLBL (R01-HL128503) and is an HHMI Investigator.

Data Availability

All images used for collateral analysis are available in the Stanford Digital Repository (https://doi.org/10.25740/qk058jq2233). Images and meshes of the adult and neonate used for computational modeling are accessible in the vascular modeling repository (https://www.vascularmodel.com/repository.html).

References

1. Go AS et al. Heart Disease and Stroke Statistics - 2014 Update: A report from the American Heart Association. Circulation vol. 129 (2014).
2. Zimarino M, D'andreamatteo M, Waksman R, Epstein SE & De Caterina R The dynamics of the coronary collateral circulation. Nature Reviews Cardiology vol. 11 191–197 (2014). [PubMed: 24395049]
3. Meier P et al. The impact of the coronary collateral circulation on outcomes in patients with acute coronary syndromes: Results from the ACUITY trial. Heart 100, 647–651 (2014). [PubMed: 24310521]
4. Yang F et al. Genetic engineering of human stem cells for enhanced angiogenesis using biodegradable polymeric nanoparticles. Proc. Natl. Acad. Sci 107, 3317–3322 (2010). [PubMed: 19805054]
5. Red-Horse K & Das S New Research Is Shining Light on How Collateral Arteries Form in the Heart: a Future Therapeutic Direction? Current Cardiology Reports vol. 23 (2021).
6. Maxwell MP, Hearse DJ & Yellon DM Species variation in the coronary collateral circulation during regional myocardial ischaemia: A critical determinant of the rate of evolution and extent of myocardial infarction. Cardiovascular Research vol. 21 737–746 (1987). [PubMed: 3440266]
7. Das S et al. A Unique Collateral Artery Development Program Promotes Neonatal Heart Regeneration. Cell 176, 1128–1142.e18 (2019). [PubMed: 30686582]
8. Zhang H & Faber JE De-novo collateral formation following acute myocardial infarction: Dependence on CCR2+ bone marrow cells. J. Mol. Cell. Cardiol 87, 4–16 (2015). [PubMed: 26254180]
9. He L et al. Genetic lineage tracing discloses arteriogenesis as the main mechanism for collateral growth in the mouse heart. Cardiovasc. Res 109, 419–430 (2016). [PubMed: 26768261]
10. Lucitti JL et al. Variants of Rab GTPase-effector binding protein-2 cause variation in the collateral circulation and severity of stroke. Stroke 47, 3022 (2016). [PubMed: 27811335]
11. Traupe T, Gloekler S, De Marchi SF, Werner GS & Seiler C Assessment of the human coronary collateral circulation. Circulation vol. 122 1210–1220 (2010). [PubMed: 20855668]
12. Rios Coronado PE & Red-Horse K Enhancing cardiovascular research with whole-organ imaging. Curr. Opin. Hematol 28, 214–220 (2021). [PubMed: 33741761]
13. Les AS et al. Quantification of hemodynamics in abdominal aortic aneurysms during rest and exercise using magnetic resonance imaging and computational fluid dynamics. Ann. Biomed. Eng 38, 1288–1313 (2010). [PubMed: 20143263]
14. Seo J, Ramachandra AB, Boyd J, Marsden AL & Kahn AM Computational Evaluation of Venous Graft Geometries in Coronary Artery Bypass Surgery. Semin. Thorac. Cardiovasc. Surg (2021) doi:10.1053/j.semtcvs.2021.03.007.

15. Min JK et al. Diagnostic Accuracy of Fractional Flow Reserve From Anatomic CT Angiography. JAMA 308, 1237–1245 (2012). [PubMed: 22922562]
16. Zhao S et al. Patient-specific computational simulation of coronary artery bifurcation stenting. Sci. Reports 2021 111 11, 1–17 (2021).
17. Shad R et al. Patient-Specific Computational Fluid Dynamics Reveal Localized Flow Patterns Predictive of Post–Left Ventricular Assist Device Aortic Incompetence. Circ. Hear. Fail 737–745 (2021) doi:10.1161/CIRCHEARTFAILURE.120.008034.
18. Su B et al. Numerical investigation of blood flow in three-dimensional porcine left anterior descending artery with various stenoses. Comput. Biol. Med 47, 130–138 (2014). [PubMed: 24607680]
19. Lindsey SE et al. Growth and hemodynamics after early embryonic aortic arch occlusion. Biomech. Model. Mechanobiol 14, 735–751 (2015). [PubMed: 25416845]
20. Vedula V et al. A method to quantify mechanobiologic forces during zebrafish cardiac development using 4-D light sheet imaging and computational modeling. PLOS Comput. Biol 13, e1005828 (2017). [PubMed: 29084212]
21. Suo J et al. Hemodynamic Shear Stresses in Mouse Aortas Implications for Atherogenesis Materials and Methods Geometry Data Acquisition of the Mouse Aorta (2007) doi:10.1161/01.ATV.0000253492.45717.46.
22. Shannon AT & Mirbod P Three-dimensional flow patterns in the feto-placental vasculature system of the mouse placenta. Microvasc. Res 111, 88–95 (2017). [PubMed: 28111314]
23. Bernabeu MO et al. Computer simulations reveal complex distribution of haemodynamic forces in a mouse retina model of angiogenesis. J. R. Soc. Interface 11, (2014).
24. Greve JM et al. Allometric scaling of wall shear stress from mice to humans: Quantification using cine phase-contrast MRI and computational fluid dynamics. Am. J. Physiol. - Hear. Circ. Physiol 291, 1700–1708 (2006).
25. Feintuch A et al. Hemodynamics in the mouse aortic arch as assessed by MRI, ultrasound, and numerical modeling. Am. J. Physiol. - Hear. Circ. Physiol 292, 884–892 (2007).
26. Acuna A et al. Computational Fluid Dynamics of Vascular Disease in Animal Models. J. Biomech. Eng 140, 0808011 (2018). [PubMed: 29570754]
27. Renier N et al. IDISCO: A simple, rapid method to immunolabel large tissue samples for volume imaging. Cell 159, 896–910 (2014). [PubMed: 25417164]
28. Renier N et al. Mapping of Brain Activity by Automated Volume Analysis of Immediate Early Genes. Cell 165, 1789–1802 (2016). [PubMed: 27238021]
29. Pan C et al. Shrinkage-mediated imaging of entire organs and organisms using uDISCO. Nat. Methods 13, 859–867 (2016). [PubMed: 27548807]
30. Feng Y et al. Bifurcation asymmetry of small coronary arteries in juvenile and adult mice. Front. Physiol 9, 519 (2018). [PubMed: 29867562]
31. Arshadi C, Günther U, Eddison M, Harrington KIS & Ferreira TA SNT: a unifying toolbox for quantification of neuronal anatomy. Nat. Methods 18, 374–377 (2021). [PubMed: 33795878]
32. Longair MH, Baker DA & Armstrong JD Simple Neurite Tracer: open source software for reconstruction, visualization and analysis of neuronal processes. Bioinformatics 27, 2453–2454 (2011). [PubMed: 21727141]
33. Updegrove A et al. SimVascular: An Open Source Pipeline for Cardiovascular Simulation. Annals of Biomedical Engineering vol. 45 525–541 (2017). [PubMed: 27933407]
34. Le VP & Wagenseil JE Echocardiographic Characterization of Postnatal Development in Mice with Reduced Arterial Elasticity. Cardiovasc. Eng. Technol 3, 424–438 (2012). [PubMed: 23646094]
35. Huo Y, Guo X & Kassab GS The flow field along the entire length of mouse aorta and primary branches. Ann. Biomed. Eng 36, 685–699 (2008). [PubMed: 18299987]
36. Vignon-Clementel IE, Figueroa CA, Jansen KE & Taylor CA Outflow boundary conditions for 3D simulations of non-periodic blood flow and pressure fields in deformable arteries. Comput. Methods Biomech. Biomed. Engin 13, 625–640 (2010). [PubMed: 20140798]

37. Kim HJ et al. Patient-Specific Modeling of Blood Flow and Pressure in Human Coronary Arteries doi:10.1007/s10439-010-0083-6.
38. Tran JS, Schiavazzi DE, Ramachandra AB, Kahn AM & Marsden AL Automated tuning for parameter identification and uncertainty quantification in multi-scale coronary simulations. Comput. Fluids 142, 128–138 (2017). [PubMed: 28163340]
39. Huang Y, Guo X & Kassab GS Axial nonuniformity of geometric and mechanical properties of mouse aorta is increased during postnatal growth. Am. J. Physiol. - Hear. Circ. Physiol 290, 657–664 (2006).
40. Seiler C, Fleisch M, Garachemani A & Meier B Coronary collateral quantitation in patients with coronary artery disease using intravascular flow velocity or pressure measurements. J. Am. Coll. Cardiol 32, 1272–1279 (1998). [PubMed: 9809936]
41. Stoner JD, Angelos MG & Clanton TL Myocardial contractile function during postischemic low-flow reperfusion: critical thresholds of NADH and O_2 delivery. Am. J. Physiol. Circ. Physiol 286, H375–H380 (2004).
42. Huang W, Yen RT, McLaurine M & Bledsoe G Morphometry of the human pulmonary vasculature 10.1152/jappl.1996.81.5.2123 81, 2123–2133 (1996).
43. Kassab GS, Rider CA, Tang NJ & Fung YCB Morphometry of pig coronary arterial trees. Am. J. Physiol. - Hear. Circ. Physiol 265, (1993).
44. Fleeter CM, Geraci G, Schiavazzi DE, Kahn AM & Marsden AL Multilevel and multifidelity uncertainty quantification for cardiovascular hemodynamics. Comput. Methods Appl. Mech. Eng 365, (2020).
45. Pfaller MR et al. Automated generation of 0D and 1D reduced-order models of patient-specific blood flow. Arxiv (2021).
46. Wustmann K, Zbinden S, Windecker S, Meier B & Seiler C Is there functional collateral flow during vascular occlusion in angiographically normal coronary arteries? Circulation 107, 2213–2220 (2003). [PubMed: 12707241]
47. Meier P et al. The collateral circulation of the heart. BMC Med. 2013 111 11, 1–7 (2013).
48. Reiner L, Molnar J, Jimenez FA & Freudenthal RR Interarterial coronary anastomoses in neonates. Arch. Pathol 71, 103–112 (1961). [PubMed: 13740594]
49. Bloor CM, Keefe JF & Browne MJ Intercoronary anastomoses in congenital heart disease. Circulation 33, 227–231 (1966). [PubMed: 25823095]
50. Kolesová H, Bartoš M, Hsieh WC, Olejníčková V & Sedmera D Novel approaches to study coronary vasculature development in mice. Dev. Dyn 247, 1018–1027 (2018). [PubMed: 29770532]
51. Kirst C et al. Mapping the Fine-Scale Organization and Plasticity of the Brain Vasculature. Cell 180, 780–795.e25 (2020). [PubMed: 32059781]
52. Mittal N et al. Analysis of blood flow in the entire coronary arterial tree. Am. J. Physiol. - Hear. Circ. Physiol 289, 439–446 (2005).
53. Huo Y et al. Growth, ageing and scaling laws of coronary arterial trees. J. R. Soc. Interface 12, (2015).
54. Hutchins GM, Miner MM & Bulkley BH Tortuosity as an index of the age and diameter increase of coronary collateral vessels in patients after acute myocardial infarction. Am. J. Cardiol 41, 210–215 (1978). [PubMed: 623014]
55. Chilian WM, Eastham CL & Marcus ML Microvascular distribution of coronary vascular resistance in beating left ventricle. Am. J. Physiol. - Hear. Circ. Physiol 251, (1986).
56. Nellis SH, Liedtke AJ & Whitesell L Small coronary vessel pressure and diameter in an intact beating rabbit heart using fixed-position and free-motion techniques. Circ. Res 49, 342–353 (1981). [PubMed: 7249271]
57. Gould KL, Lipscomb K & Calvert C Compensatory changes of the distal coronary vascular bed during progressive coronary constriction. Circulation 51, 1085–1094 (1975). [PubMed: 1132098]
58. Dick GM, Namani R, Patel B & Kassab GS Role of Coronary Myogenic Response in Pressure-Flow Autoregulation in Swine: A Meta-Analysis With Coronary Flow Modeling. Front. Physiol 9, 580 (2018). [PubMed: 29875686]

59. Shalman E, Rosenfeld M, Dgany E & Einav S Numerical modeling of the flow in stenosed coronary artery. The relationship between main hemodynamic parameters. Comput. Biol. Med 32, 329–344 (2002). [PubMed: 12102752]

Method References

60. Malkasian S, Hubbard L, Dertli B, Kwon J & Molloi S Quantification of vessel-specific coronary perfusion territories using minimum-cost path assignment and computed tomography angiography: Validation in a swine model. J. Cardiovasc. Comput. Tomogr 12, 425–435 (2018). [PubMed: 30042078]

61. Van Doormaal MA et al. Haemodynamics in the mouse aortic arch computed from MRI-derived velocities at the aortic root. J. R. Soc. Interface 9, 2834–2844 (2012). [PubMed: 22764131]

62. Hartley CJ, Reddy AK, Michael LH, Entman ML & Taffet GE Coronary flow reserve as an index of cardiac function in mice with cardiovascular abnormalities. in 2009 Annual International Conference of the IEEE Engineering in Medicine and Biology Society 1094–1097 (IEEE, 2009). doi:10.1109/IEMBS.2009.5332488.

63. Sankaran S et al. Patient-specific multiscale modeling of blood flow for coronary artery bypass graft surgery. Ann. Biomed. Eng 40, 2228–2242 (2012). [PubMed: 22539149]

64. Fåhræus R & Lindqvist T THE VISCOSITY OF THE BLOOD IN NARROW CAPILLARY TUBES. Am. J. Physiol. Content 96, 562–568 (1931).

65. Kassab GS, Rider CA, Tang NJ & Fung YCB Morphometry of pig coronary arterial trees. Am. J. Physiol. - Hear. Circ. Physiol 265, (1993).

66. Dong M et al. Image-based scaling laws for somatic growth and pulmonary artery morphometry from infancy to adulthood. Am. J. Physiol. - Hear. Circ. Physiol 319, H432–H442 (2020).

67. Raftrey B et al. Dach1 Extends Artery Networks and Protects Against Cardiac Injury. Circ. Res (2021) doi:10.1161/circresaha.120.318271.

68. Yardeni T, Eckhaus M, Morris HD, Huizing M & Hoogstraten-Miller S Retro-orbital injections in mice. Lab Anim. (NY) 40, 155 (2011). [PubMed: 21508954]

69. Cunningham FG et al. Abortion. in Williams Obstetrics, 25e (McGraw-Hill Education, 2018).

70. Cunningham FG et al. Prenatal Care. in Williams Obstetrics, 25e (McGraw-Hill Education, 2018).

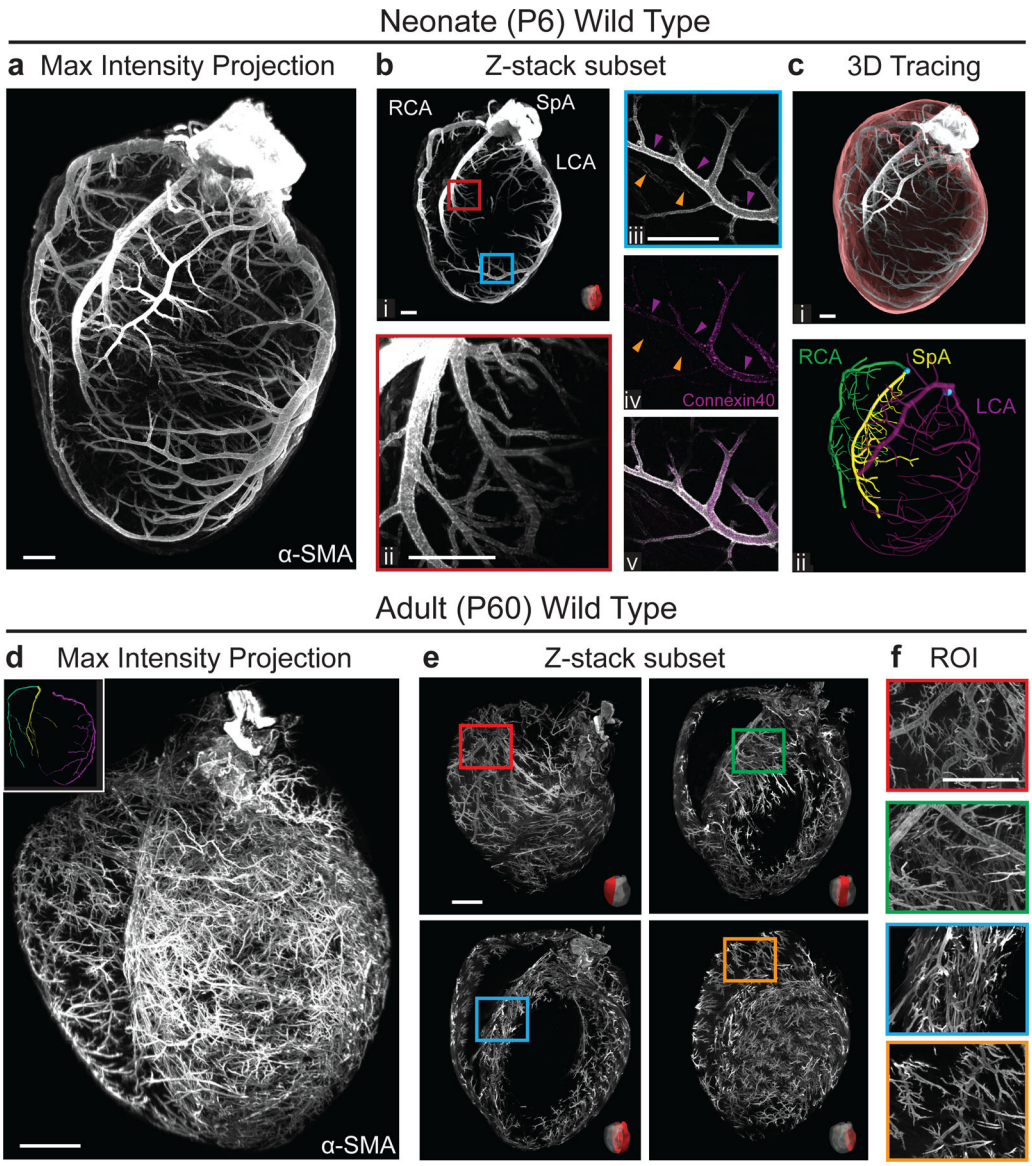

Figure 1: Whole-organ imaging of coronary arteries at cellular resolution.

Neonate and adult hearts (atria removed) subjected to tissue clearing and immunolabeling with alpha-smooth muscle actin (α-SMA) and imaged using a Light sheet microscope. (**a**) Maximum intensity projection of entire neonate heart. (**b**) Z-Stack subset projections of Light sheet images (**b_{i-ii}**) or those captured using a confocal microscope (**b_{iii-v}**). High magnification of septum shows complexity of the septal artery (**b_{iii}**) and of LCA shows colocalization of α-SMA+ branches with artery marker Connexin40 (purple arrowheads, similar results found in n=40 hearts)(**b_{iii-v}**). An α-SMA^{low}Connexin40- vein (orange arrowheads) is also present in **b_{iii-v}**. (**c**) 3D rendering of myocardial volume (red)(**c_i**) and main coronary artery branches: Right, Septal and Left (**c_{ii}**). (**d**) Maximum intensity projection of entire adult heart. Upper left corner shows 3D rendering of main coronary artery branches similarly as in **c_{ii}**. (**e** and **f**) Z-Stack subsets of indicated heart regions (**e**) and region-of-interest (ROI) images (**f**) reveal the high resolution and specificity of

immunolabeling with this technique. LCA, left coronary artery; RCA, right coronary artery; SpA, septal coronary artery. Scale bars: **a-c**, 300 μm; **d-f**, 500 μm.

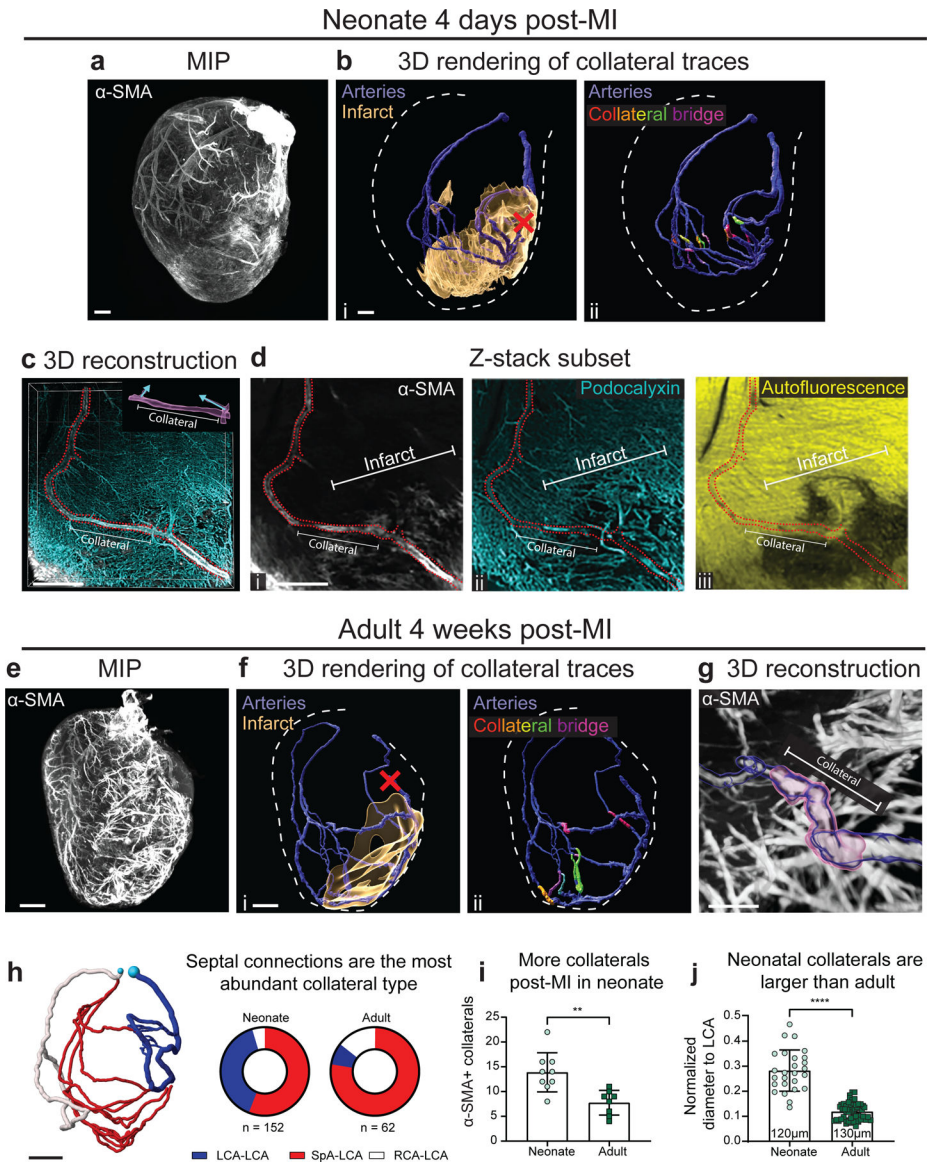

Figure 2: Increased collateral arteries in neonate versus adult hearts post injury.

(**a-d**) Whole organ imaging of P6 neonatal heart labeled with α-SMA post myocardial infarction (MI). (**a**) Maximum intensity projection (MIP) of entire heart. (**b**) Collateral connections traced from downstream of suture (red X) were 3D rendered and overlaid with infarct volume (**b_i**) and collateral bridges (**b_{ii}**). (**c**) 3D reconstruction of 100 μm Z-stack containing a representative collateral bridge within a traced vessel (red dotted line). (**d**) MIP of a 35 μm Z-stack within **c** highlighting an α-SMA+ collateral (**d_i**) and its relation to Podocalyxin labeling all vessels (**d_{ii}**) and Autofluorescence labeling surviving myocardium (**d_{iii}**). (**e-g**) Adult (16-week-old) injured hearts labeled with α-SMA. (**e**) MIP of entire heart. (**f**) 3D rendering of collateral connections overlaid with infarct volume (**f_i**) or collateral bridges (**f_{ii}**). (**g**) 3D reconstruction of representative collateral bridge (pink). (**h**) Classification and distribution of collateral connections. (**i**) Collateral numbers in neonate (n=9 hearts) and adult (n=8 hearts) post-MI. (**j**) Collateral diameters in neonate (n=26

collaterals, n=3 hearts) and adult (n=55 collaterals, n=8 hearts) post-MI normalized to the proximal LCA. Scale bars: **a-b** and **e-f**, 300 μm; **c-d** and **g-h**, 150 μm. Right (RCA), left (LCA), and septal (SpA) coronary arteries. Error bars are mean ± st dev: **, p= 0.0019; ****, p= <0.0001 by two-sided Student's t-test.

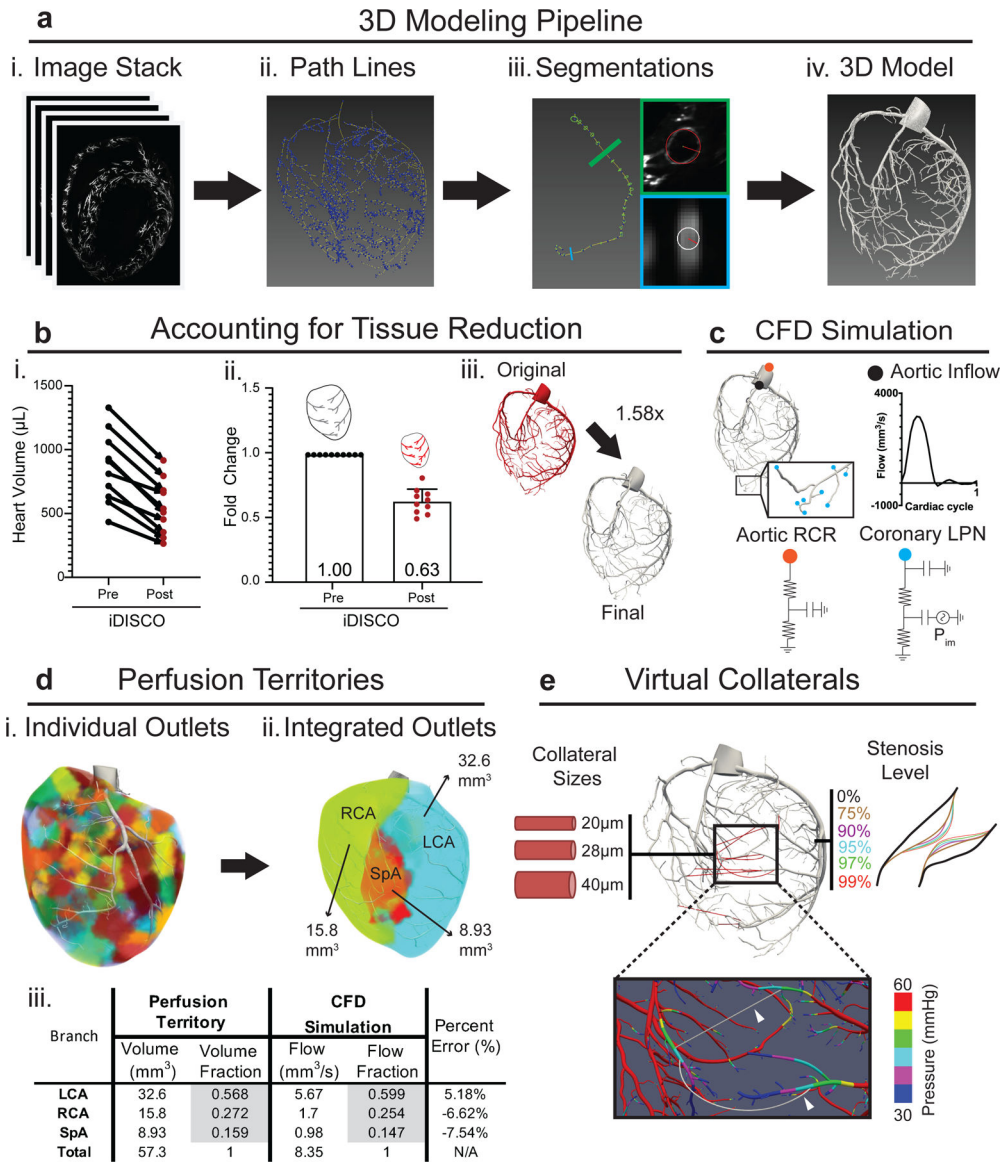

Branch	Perfusion Territory		CFD Simulation		Percent Error (%)
	Volume (mm^3)	Volume Fraction	Flow (mm^3/s)	Flow Fraction	
LCA	32.6	0.568	5.67	0.599	5.18%
RCA	15.8	0.272	1.7	0.254	-6.62%
SpA	8.93	0.159	0.98	0.147	-7.54%
Total	57.3	1	8.35	1	N/A

Figure 3: Building a physiologically representative 3D model of mouse coronary arteries.

(**a**) Pipeline for generating 3D models from Light sheet images. (**b**) Scaling model to account for tissue volume reduction during iDISCO procedure. Measuring heart volumes (n = 10 hearts) pre- and post-processing (**b_i**) yielded an average reduction value (**b_{ii}**) used to generate a scaling factor for models (**b_{iii}**). (**c**) Schematic of coronary simulation with a prescribed flow waveform at the inlet, RCR boundary condition at the aortic outlet, and coronary LPN at each coronary outlet. (**d**) Determining perfusion territories required first utilizing the Voronoi algorithm to outline perfusion subvolumes for each individual outlet (colors in **d_i**). Then, subvolumes were grouped by right (RCA), left (LCA), and septal (SpA) coronary branches (**d_{ii}**). Outlet boundary conditions were tuned by matching simulated flow splits to perfusion territories (**d_{iii}**). (**e**) Schematic depicting variations on collateral and stenosis parameters used in this study. Collaterals were placed to connect approximately

equal pressure zones (white arrows). RCR, 3-element Windkessel model; LPN, lumped parameter network; P_{im}, intramyocardial pressure.

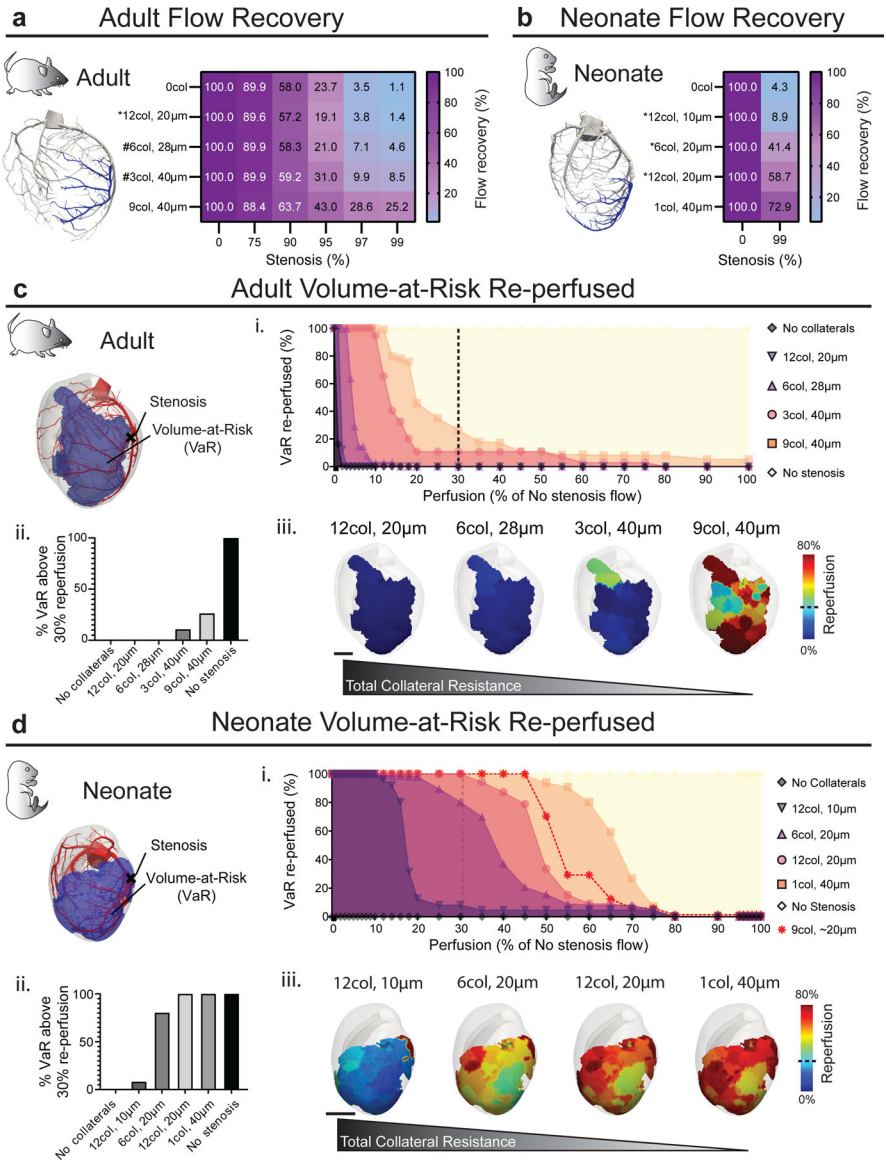

Figure 4: Collateral arteries are predicted to perform better in neonate hearts.

(**a** and **b**) Measuring re-perfusion capacity by calculating percent of total non-stenotic flow in vessels downstream of the virtual occlusion (blue vessels). Asterisks denote configurations observed experimentally; hashtags denote sizes observed in previous study[7]. Functionally significant re-perfusion is only seen in neonates under physiological conditions. (**c** and **d**) Percent re-perfusion of myocardial volume-at-risk (VaR)(blue region) in adult (**c**) and neonatal (**d**) models. Cumulative histogram ($\mathbf{c_i}$, $\mathbf{d_i}$), bar graph of percent VaRs above 30% ($\mathbf{c_{ii}}$, $\mathbf{d_{ii}}$), and visual maps of re-perfusion within the VaR ($\mathbf{c_{iii}}$, $\mathbf{d_{iii}}$). Black dotted line marks the ischemia threshold of 30% non-stenotic flow. The red dotted line represents re-perfusion within VaR of *in vivo* collaterals formed in response to MI in neonate ($\mathbf{d_i}$). Scale bar: 1000 µm.

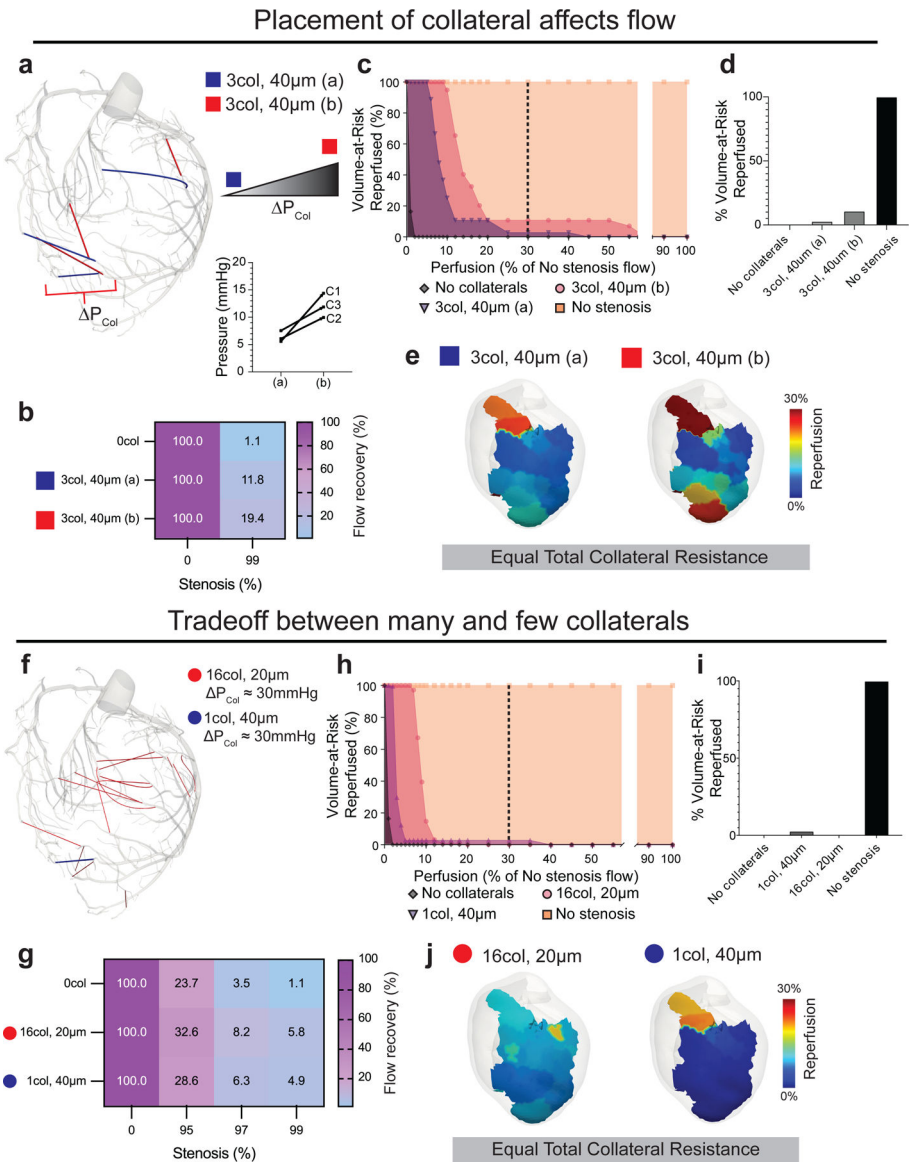

Figure 5: Evaluating collateral placement and the tradeoff between collateral number and size.

(**a-e**) Investigating how collateral placement affects re-perfusion using two collateral configurations. (**a**) 3 collaterals with either high (red square) or low ΔP_{Col} (blue square). (**a**) Graph showing the ΔP_{Col} changes caused by altering placement for each collateral. (**f-j**) Investigating re-perfusion tradeoff between many, small and few, large collaterals using two configurations: 16 collaterals at 20µm (red circle) and 1 collateral at 40µm (blue circle). (**b, g**) The total non-stenotic flow in vessels downstream of the virtual occlusion. Cumulative histogram (**c, h**), bar graph of percent volume-at-risk (VaR) above 30% (**d, i**), and visual maps of re-perfusion within the VaR (**e, j**). Dotted line marks the ischemia threshold of 30% non-stenotic flow. ΔP_{Col}, pressure difference across collaterals.

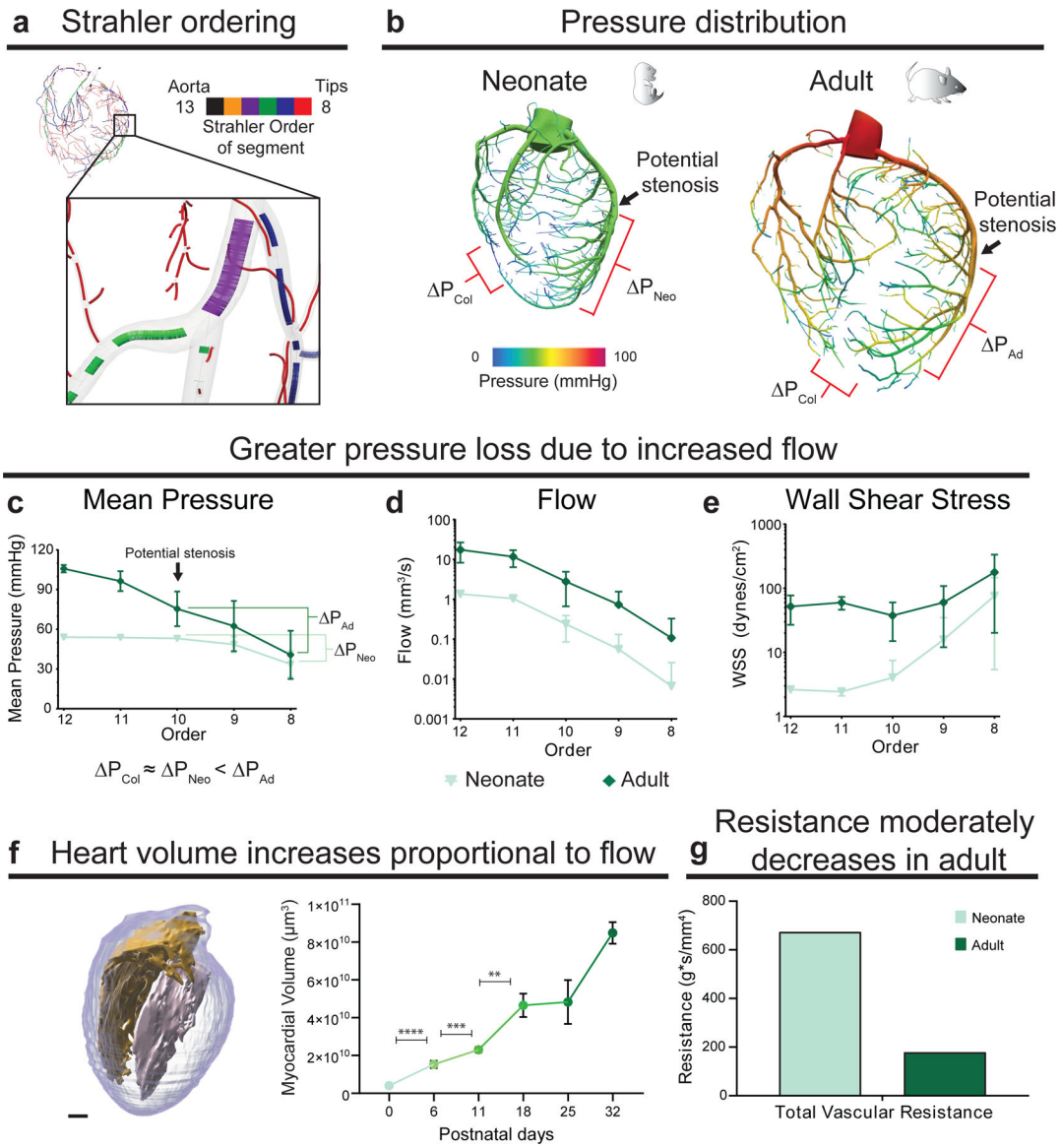

Figure 6: Investigating hemodynamic differences between neonate and adult.

(**a**) Strahler ordering categorizes segments of the arterial tree from order 13 (aorta) to order 8 (distal tips). (**b**) Pressure distribution in the neonate and adult coronary models. (**c-e**) Quantification of pressure (**c**), flow (**d**), and wall shear stress (**e**) vs. Strahler order (n=1 P6, n=1 P60 heart model). (**f**) Heart volume segmentation (left) and quantification (n=3 P0, n=7 P6, n=3 P11, n=2 P18, n=2 P25, n=2 P32 hearts). (**g**) Total 3D resistance of the coronary tree in neonate and the adult models revealed a 3-fold decrease in adults. ΔP_{Col}, pressure difference across collaterals; pressure difference downstream of a potential stenosis in the neonate, ΔP_{Neo}, and the adult, ΔP_{Ad}. Error bars are mean ± st dev: **, p=0.0062; ***, p=0.0003; ****, p=<0.0001 by two-sided Student's t-test.

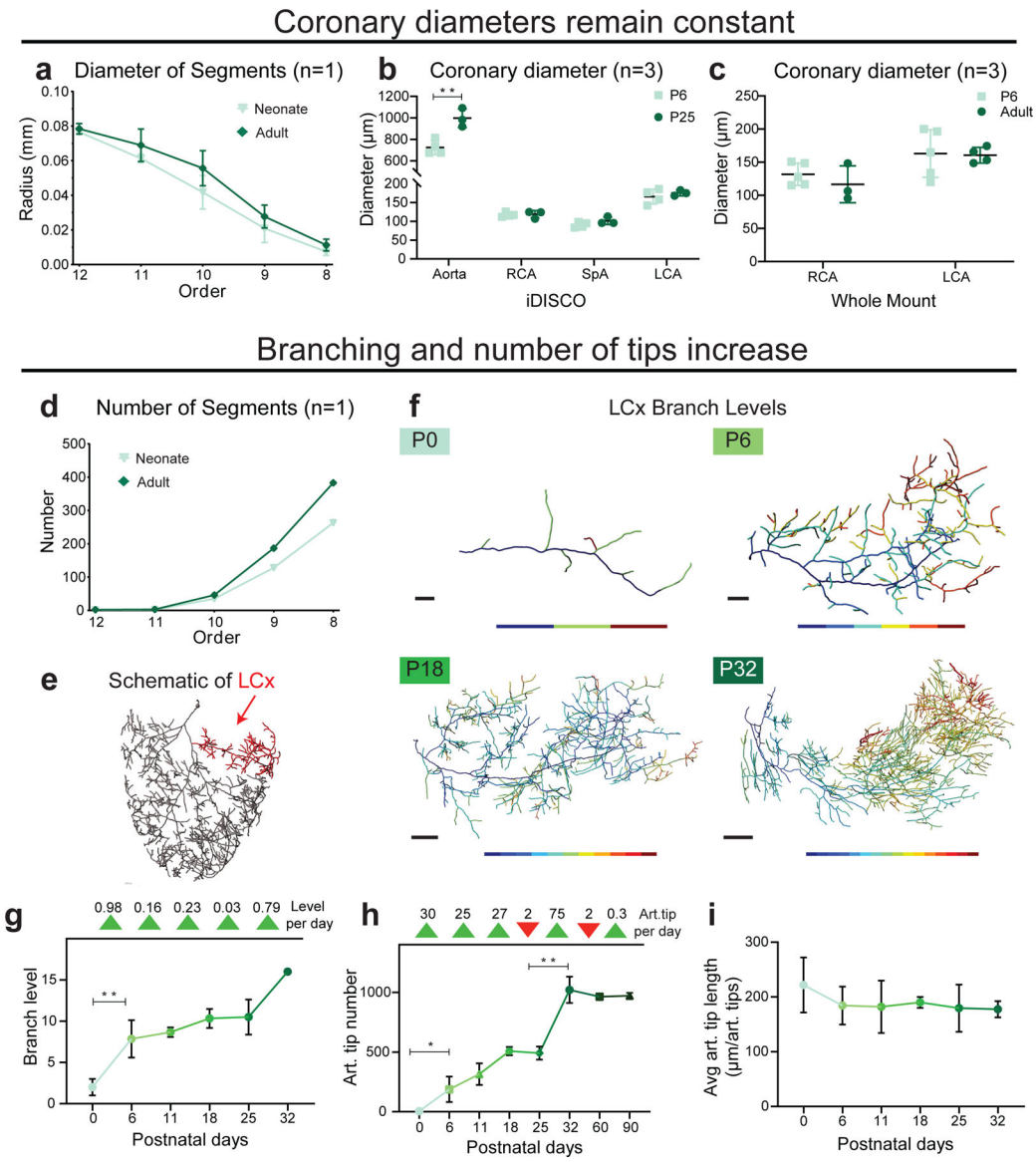

Figure 7: Main branch coronary artery diameters remain constant while branching increases throughout postnatal development.

(**a**) Quantification of diameter vs. Strahler order. (**b** and **c**) Main branch coronary diameter measurements from additional hearts processed through iDISCO (**b**) or conventional whole mount immunostaining without clearing (**c**). (**d**) Number of artery segments per Strahler order. (**e**) Semi-manual segmentation of LCA, highlighting the left coronary circumflex branch (LCx, red). (**f**) Visual representation of branch levels in 3D reconstructed LCx traces. (**g**) Number of branch levels of LCx at each timepoint. Arrowheads indicate rate of change per day. (**h**) Number of arterial (art.) tips in the LCx at each age. Arrowheads indicate rate of change per day. (**i**) Average art. segment length in LCx at each timepoint. (**a**,**d**) n=1 P6, n=1 P60 hearts; (**b**) n=4 P6, n=3 P25 hearts; (**c**) n=5 P6, n= 4 P60 hearts; (**g**,**h**,**i**) n=3 P0, n=7 P6, n=3 P11, n=2 P18, n=2 P25, n=2 P32 hearts. Changes in green color tonality denote increment in age. (**h**,**i**) n=1 P60, n=2 P90 hearts. Scale bars: **f**, P0, 100 µm; P6, 200 µm;

P18, 400 μm; P32, 500 μm. Error bars are mean ± st dev: **, p=0.0030 (**g**); *, p= 0.0216 (**h**, P0-P6); **, p=0.0017 (**h**, P25–32) by two-sided Student's t-test.

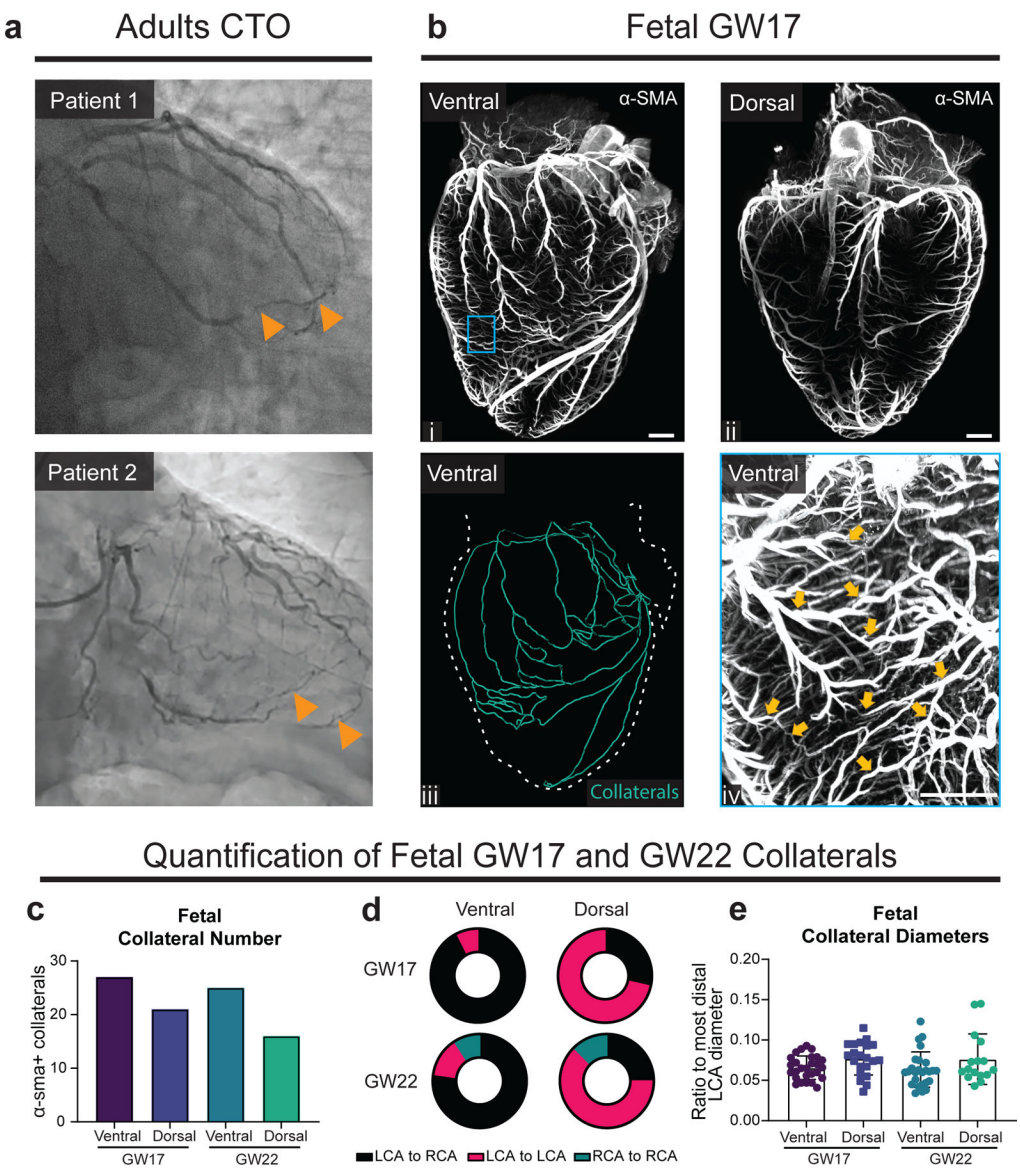

Figure 8: Collateral arteries in adult and fetal human hearts.

(**a**) Representative invasive angiograms from adult chronic total occlusion (CTO) patients. Orange arrowheads indicate collaterals. (**b_{i-ii}**) Maximum intensity projections of fetal human heart, ventral (**b_i**) and dorsal (**b_{i-ii}**) sides. (**b_{iii}**) Traced collateral connections on the ventral side. (**b_{iv}**) High magnification (boxed in **b_i**) of collateral bridges (arrowheads). (**c**-**e**) Quantification of collateral bridge numbers (n=27 ventral, n=21 dorsal collaterals, n=1 GW17 heart; n=26 ventral, n=16 dorsal collaterals, n=1 GW22 heart) (**c**), connection types (**d**), and diameters (**e**). GW, gestational week. Error bars are mean ± st dev. Scale bars: 1 mm.